This is the peer reviewed version of the following article: Lam, G. C. Y., & Leung, R. C. K. (2018). Aeroacoustics of NACA 0018 Airfoil with a Cavity. AIAA Journal, 56(12), 4775-4786, which has been published in final form at https://doi.org/10.2514/1.J056389.

Aeroacoustics of NACA 0018 Airfoil with a Cavity

Garret C. Y. Lam[1] and Randolph C. K. Leung[2]
The Hong Kong Polytechnic University, Hong Kong, P. R. China

This paper reports a detailed numerical study of the aeroacoustics of NACA 0018 airfoil with a cavity at zero angle of attack, with chord based Reynolds and free-stream Mach numbers at 2×10^4 and 0.2, in two dimensions. For an airfoil without a cavity, vortex shedding from trailing edge and low-frequency wake flapping are found to be the major aeroacoustic processes. The presence of a cavity introduces additional acoustic generation due to cavity oscillation modes but weakens the noise source at the airfoil trailing edge via a jittering of flow. Three aeroacoustic mechanisms are identified with extensive FFT, wavelet and coherence analyses. The airfoil with cavity effectively increases the lift-to-drag ratio from almost zero (ordinary airfoil) to approximately 5.3. However, it radiates less acoustic power by 1.2 dB, and by 2.6 dB respectively from airfoil upper and lower surfaces even if the contribution of wake flapping of ordinary airfoil is excluded. The outcomes of the study suggest that an airfoil with a cavity is a feasible configuration that gives high lift-to-drag ratio yet low noise generation, making it a promising quiet airfoil design at low Reynolds number.

---

[1] Research Fellow, Department of Mechanical Engineering, garret.lam.hk@connect.polyu.hk
[2] Associate Professor, Department of Mechanical Engineering, mmrleung@polyu.edu.hk, and Senior AIAA Member.

Nomenclature

c = Acoustic speed

$\overline{C_D}$, $\overline{C_L}$, $\overline{C_P}$ = Time averaged drag, lift and pressure coefficient

$C'_{D,rms}$, $C'_{L,rms}$ = Root mean squared fluctuations of drag, lift coefficient

D = Depth of cavity

E = Energy

f = Frequency

$f_{v,\mathrm{CAV},0}$ = Fundamental vortex shedding frequency at airfoil trailing edge in CAV

$f_{v,\mathrm{CAV},n}$ = $(n+1) \times f_{v,\mathrm{CAV},0}$

$f_{v,\mathrm{OA},0}$ = Fundamental vortex shedding frequency at airfoil trailing edge in OA

$f_{v,\mathrm{OA},n}$ = $(n+1) \times f_{v,\mathrm{OA},0}$

L = Chord length

L_d = Distance of the flow disturbances traveling in the feedback loop

M = Mach number

P = FFT spectral power

p = Pressure

r = Distance from airfoil trailing edge

r_T = Thermal recovery factor

Re = Chord based Reynolds number

St = Strouhal number

$St_{W,n}$ = Strouhal number of the n-th Rossiter mode based on W

T = Temperature

t = Time

u, v = Velocities in $x-$ and $y-$ direction

U_∞ = Free stream flow velocity

v_c = Disturbance convective speed

W = Width of cavity

W_{AB} = Cross wavelet spectrum of probes A and B

α = Angle of attack

γ = Specific heat ratio

η = Time parameter in wavelet analysis

θ = Angle measured from x-axis

θ_o = Momentum thickness of boundary layer at the leading edge of cavity

κ = Average convective speed of shear layer disturbances

μ = Viscosity

ρ = Density

φ = Phase delay in Rossiter mode calculation

Ψ = Morlet wavelet function

ω_o = Central frequency in wavelet analysis

$\overline{\phi}$ = Time averaged value of quantity ϕ

ϕ' = Fluctuation of quantity ϕ

ϕ_{rms} = Root mean squared value of quantity ϕ

ϕ_∞ = Quantity ϕ at free stream

I. Introduction

Low Reynolds number flow over airfoil has long been a hot topic of research interest due to its popular applications in small engineering systems e.g. small wind turbines and micro air vehicle (MAV). In these applications, the chord based Reynolds number Re can be as low as the order of 10^4 [1–3]. Previous research was usually focused on the flow evolution in the light of obtaining improved airfoil aerodynamic performance. Researchers also aim at exploring an innovative airfoil configuration which produces strong lift but weak noise during system operation.

One of the design variations showing a high potential is a thick airfoil with a cavity mounted on its suction surface, which is borrowed from original Kasper's wing [4] for the enhancement of aircraft lift. This concept has favorable features over the conventional airfoil design in three aspects. Firstly, it supports a simple and strong airfoil box structure. Secondly, according to the potential flow theory [5] , it easily creates a favorable pressure gradient over the entire airfoil by trapping two counter-rotating vortices inside the cavity. Thirdly, the trapped vortices in the vicinity of the airfoil suction surface not only provide an extra low pressure region for airfoil lift enhancement, but also favorably produces a lower drag. Since the introduction of Kasper's wing, there were studies dedicated to controlling the flow development inside the cavity for the gain in performance in the real aviation [5–11]. For instance, Tutty et al. [11] adopted a constant suction in the cavity region to suppress large-scale unsteady motion of an airfoil at $Re \sim 10^6$ and thus successfully stabilized the trapped vortex in the cavity.

There are only a few studies in low Re flow of airfoil with cavity. Recently, Olsman et al. [12, 13] have studied the flow past a NACA 0018 with a cavity at various angles of attack α. They also performed experiments in water tunnel to visualize the unsteady flow behavior. Their results reveal the existence of two different cavity shear layer modes at various angles of attack α. Mode switching also occurs at certain α (e.g. 0°). Furthermore, the cavity may reduce extensive flow separation downstream due to the passage of (cavity generating) vortices over it. It is interesting to note from their numerical results that there is a possibility of attaining a higher lift-to-drag ratio than that of ordinary airfoil. They further investigated the receptivity of the airfoil using acoustic forcing at different values of Re [12]. Natural instability modes were observed under acoustic forcing at low $Re \sim O\left(10^4\right)$, rather than at higher $Re > 10^5$.

The acoustics of the airfoil with cavity at low Re received almost no attention. The experimental work of Schumacher et al. [14] with a thin plate with super-elliptic nose and tapered tail at $Re \sim O\left(10^5\right)$ is the closest in scope. They measured the far field tonal noise and the velocity fluctuations inside the shear layer of the cavity with microphones and hot-wire anemometry for $7 \times 10^4 < Re < 3.2 \times 10^5$ with cavity at various locations, and compared the spectra. Their results suggested that the acoustic feedback loop between the cavity and the airfoil trailing edge is the root cause for tonal noise production in various flow conditions. More specifically, the instability of the boundary layer downstream of the cavity is mainly responsible for the airfoil tones. However, the relationship between the cavity flow dynamics and the aerodynamic noise generation of the plate was not investigated in details. It is still not clearly understood.

Therefore, we aim at bridging this knowledge gap by means of a detailed numerical study starting with a simple yet representative case. The NACA 0018 airfoil with cavity adopted in the work of Olsman and Colonius [13] was proven able to sustain trapped vortices in the cavity without the need of any active control technique based on localized blowing and suction. It was also found exhibiting an increase in lift-to-drag ratio. There is substantial information of its aerodynamics available [12, 13] for comparison. Therefore, the same NACA 0018 airfoil and same flow condition (i.e. $Re = 2 \times 10^4$) are selected in the present study. We concentrate our effort on $\alpha = 0^\circ$ for its reported strong prevalence of shear layer modes of cavity and a wide range of interesting unsteady aerodynamics they induced. We compare its aerodynamics and the acoustic generation with those of NACA 0018 airfoil without cavity so as to delineate the effect of the cavity on the acoustics.

This paper is organized as follows. Section II describes the formulation of the problem and the numerical methodology adopted in the present study. Then in Section III, the discussions on the aerodynamics of the airfoil are given followed by those on the airfoil acoustic generation. The results of airfoil with cavity are compared with those of the ordinary airfoil. The relationship between the acoustic generation and underlying aerodynamics is sought eventually.

II. Formulation of the Problem

A. Direct Aeroacoustic Simulation

In the present study, we adopt the direct aeroacoustic simulation (DAS) approach [15, 16] for its capability of resolving the coupling between the unsteady airfoil aerodynamic and acoustic solutions. This capability is particularly important for the investigation of those aeroacoustic problems, which might involve various feedback mechanisms between the airfoil acoustics and its generating aerodynamics [16, 17]. The conservation element and solution element (CE/SE) method is adopted in DAS to solve the evolution of scale-disparate aerodynamic and acoustic processes of the problem. Since its introduction, CE/SE method has been successfully applied in investigating aeroacoustics of compressible flows such as jet screech [19, 20]. Lam et al. [15] systemically consolidated its capability of capturing interactions between flow and acoustics accurately in a class of benchmark aeroacoustic problems at low Mach number.

1. Governing Equations

A two dimensional flow past a NACA 0018 airfoil, with or without cavity, is governed by the compressible Navier-Stokes (N-S) equations and the equation of state for calorically perfect gas. Denoting the dimensional variables with hat $\hat{}$ and those without as their normalized counterparts, and taking such reference scales as length $\widehat{L}$, velocity $\widehat{U_\infty}$, density $\widehat{\rho}_\infty$, dynamic pressure $\widehat{\rho}_\infty \widehat{U}_\infty^2$, temperature $\widehat{T}_\infty$ and viscosity $\widehat{\mu}_\infty$ from the free stream, the non-dimensionalized N-S equations can be written in strong conservation form as

$$\frac{\partial \boldsymbol{U}}{\partial t} + \frac{\partial \left(\boldsymbol{F} - \boldsymbol{F_v}\right)}{\partial x} + \frac{\partial \left(\boldsymbol{G} - \boldsymbol{G_v}\right)}{\partial y} = 0, \tag{1}$$

where $\boldsymbol{U} = \begin{bmatrix} \rho & \rho u & \rho v & \rho E \end{bmatrix}^{\mathrm{T}}$, $\boldsymbol{F} = \begin{bmatrix} \rho u & \rho u^2 + p & \rho u v & \left(\rho E + p\right) u \end{bmatrix}^{\mathrm{T}}$, $\boldsymbol{G} = \begin{bmatrix} \rho v & \rho u v & \rho v^2 + p & \left(\rho E + p\right) v \end{bmatrix}^{\mathrm{T}}$, $\boldsymbol{F_v} = \begin{bmatrix} 0 & \tau_{xx} & \tau_{xy} & \alpha_x \end{bmatrix}^{\mathrm{T}} / Re_\infty$, $\boldsymbol{G_v} = \begin{bmatrix} 0 & \tau_{xy} & \tau_{yy} & \alpha_y \end{bmatrix}^{\mathrm{T}} / Re_\infty$ with u and v being the velocities in x and y directions respectively, $\alpha_x = \tau_{xx} u + \tau_{xy} v - q_x$, $\alpha_y = \tau_{xy} u + \tau_{yy} v - q_y$, $\tau_{xx} = \frac{2}{3}\mu \left(2\frac{\partial u}{\partial x} - \frac{\partial v}{\partial y}\right)$, $\tau_{xy} = \mu \left(\frac{\partial u}{\partial y} + \frac{\partial v}{\partial x}\right)$, $\tau_{yy} = \frac{2}{3}\mu \left(2\frac{\partial v}{\partial y} - \frac{\partial u}{\partial x}\right)$, $E = \frac{p}{\rho(\gamma-1)} + \frac{u^2+v^2}{2}$, $p = \frac{\rho T}{\gamma M_\infty^2}$, $q_x = -\frac{\mu}{(\gamma-1) Pr_\infty M_\infty^2} \frac{\partial T}{\partial x}$, $q_y = -\frac{\mu}{(\gamma-1) Pr_\infty M_\infty^2} \frac{\partial T}{\partial y}$, the specific heat ratio $\gamma = 1.4$, free stream Mach number $M_\infty = \widehat{U}_\infty / \sqrt{\gamma \widehat{R} \widehat{T}_\infty}$, specific gas constant $\widehat{R} = 287.058 J / \left(kgK\right)$ for air, $Re_\infty = \widehat{\rho}_\infty \widehat{U}_\infty \widehat{L} / \widehat{\mu}_\infty$ and Prandtl number $Pr_\infty = \widehat{c_{p,\infty}} \widehat{\mu}_\infty / \widehat{k}_\infty = 0.71$.

B. Numerical Setup

In the present study, we denote the calculations of ordinary airfoil and airfoil with cavity as OA and CAV respectively. The computational domain is depicted in Fig. 1. The airfoil with cavity is a replicate of the airfoil adopted by Olsman [10]. The dimensions of cavity are $\widehat{W} = 0.21\widehat{L}$ and $\widehat{D} = 0.16\widehat{L}$. The airfoil geometry follows the description given in Ref. [21]. A uniform free-stream flow with $M_\infty = 0.2$ and $Re_\infty = 2 \times 10^4$ sweeps through the initially stagnant computational domain for time-marching the solution. An exponentially grid-stretched buffer zone [15] surrounding the whole physical domain is set to eliminate erroneous numerical reflection. All open domain boundaries adopt non-reflecting boundary condition except the left inlet boundary. On the airfoil, no-slip wall condition using near wall approach is applied [15]. CAV are performed using two meshes, namely Mesh A and its refined version Mesh B (Table 1). However, OA is performed with using Mesh A settings only (Table 1). Generally, the meshes are clustered near the airfoil and stretched towards

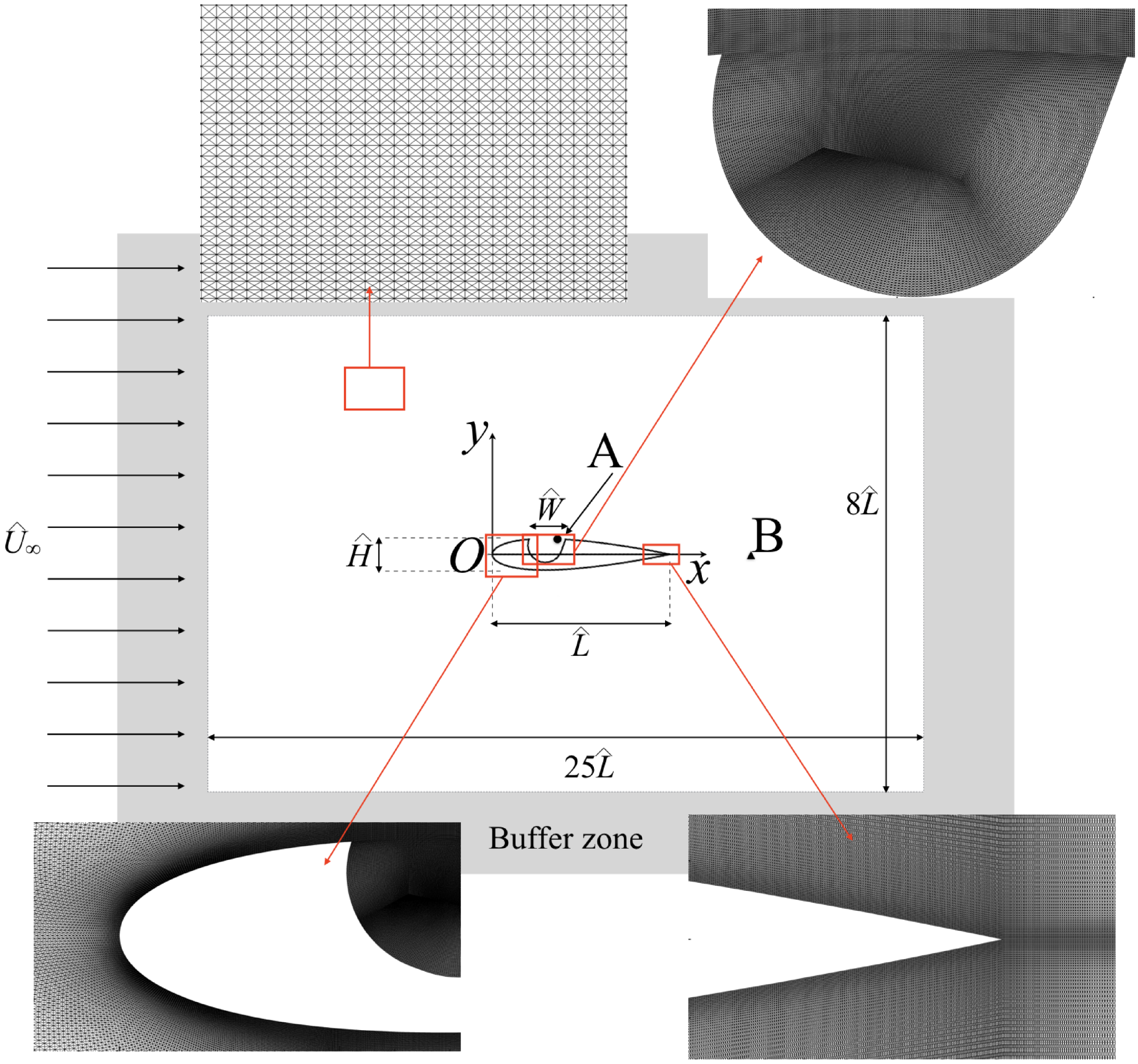

Fig. 1 Schematic sketch of the computational domain with mesh design of critical regions. ●, Probe A; ▲, probe B.

the domain boundary. The designs of some critical regions are also illustrated in Fig. 1. The time step sizes adopted for OA, CAV with Mesh A and CAV with Mesh B are 1×10^{-4}, 6.25×10^{-5} and 4×10^{-5} respectively. In this paper, all the results and analyses are undertaken with data captured within a duration of $T = 20$ after the calculations have reached time-stationarity. Probes A and B, at $(x, y) = (0.388, 0.086)$ and $(1.5, 0.0)$ respectively, are set for spectral analyses of vortex shedding inside the cavity and of the airfoil wake.

Table 1 Mesh parameters (Minimum mesh size/Maximum mesh size).

	Physical domain					Buffer zone
Mesh	$x < -1$	$-1 \leq x \leq 2$	$x > 2$	$\lvert y \rvert > 0.3$	$-0.3 \leq y \leq 0.3$	$\forall x, y$
A	0.01/0.05	0.001/0.01	0.01/0.02	0.01/0.05	0.001/0.01	0.05/1.6
B	0.0067/0.033	0.00067/0.067	0.0067/0.013	0.0067/0.033	0.00067/0.067	0.033/1.6

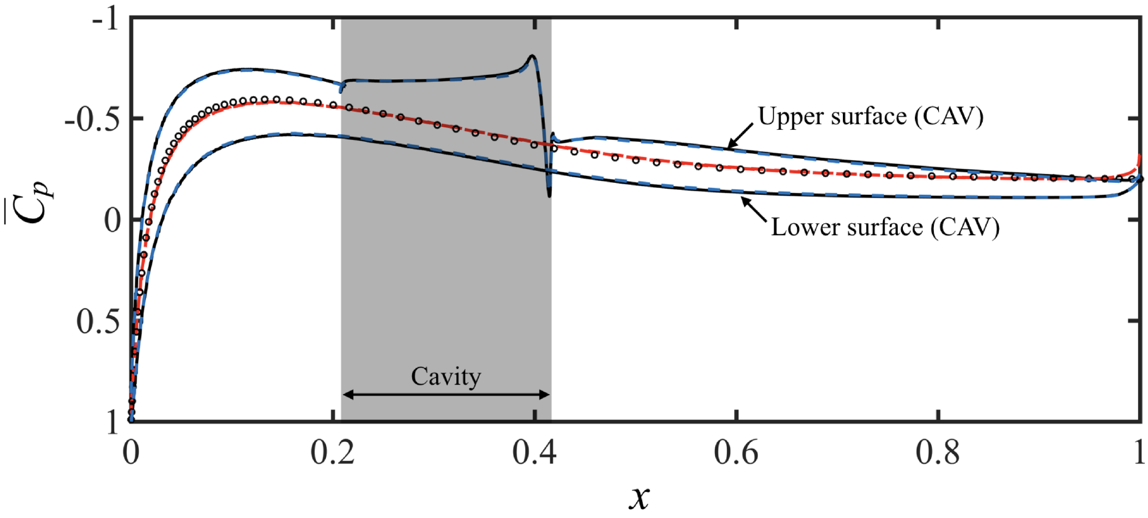

Fig. 2 Time averaged pressure coefficient $\overline{C_p}$. —, CAV (Mesh A); blue - - -, CAV (Mesh B); red - - -, OA; ○, XFoil prediction result.

III. Results and Discussions

A. Time-Averaged Aerodynamics

Fig. 2 shows the time averaged pressure coefficient $\overline{C_p} = 2\left(\overline{p} - p_\infty\right)/\rho U_\infty^2$. $\overline{C_p}$ in OA exhibits a symmetric distribution which agrees with the XFoil [22] prediction very well. In CAV, results of both meshes show insignificant difference. $\overline{C_p}$ on the lower surface decreases smoothly from the stagnation at the airfoil leading edge up to $\sim 15\%$ chord, increases slowly up to $\sim 97\%$ chord, and then decreases again. $\overline{C_p}$ on the upper surface shows a similar trend with a lower value except the abrupt changes in the region of the cavity. It decreases throughout the cavity, reaches its minimum at $x \sim 0.4$ and jumps sharply near its trailing edge.

Table 2 shows the time averaged lift coefficient $\overline{C_L}$ and drag coefficient $\overline{C_D}$ of all calculations. All these values closely match those of Olsman and Colonius [13]. The values obtained from Mesh A and B are almost the same. $\overline{C_L}$ in OA is much lower than that in CAV as expected. Unlike the

Table 2 lift, drag coefficient and Strouhal numbers St at Probe B.

	$\overline{C_L}$	$C'_{L,rms}$	$\overline{C_D}$	$C'_{D,rms}$	St_H	$St_{H,LFO}$
OA	-0.0008	0.175	0.047	0.001	0.42	~ 0.01
OA (Olsman [13])	~ -0.05	–	0.047	–	0.42	~ 0.01
CAV, Mesh A	0.238	0.056	0.045	0.022	0.39	–
CAV, Mesh B	0.234	0.060	0.045	0.022	0.39	–
CAV (Olsman [13])	~ 0.210	–	~ 0.046	–	0.43	–

nearly circular cavity adopted in Lasagna et al. [8], the inclusion of cavity does not induce extra drag to the airfoil which may be caused by vortex ejection from the cavity. This implies a high sensitivity of such drag reduction to flow conditions and geometry of the cavity. The effect of cavity on drag reduction thus requires further investigation. Present results clearly demonstrate that the presence of cavity greatly enhances the airfoil lift-to-drag ratio from almost 0 to a high value of 5.3. $C'_{L,rms}$ in OA is much higher than that in CAV because of a low frequency wake flapping in OA, which will be explored in Section III B. Furthermore, $C'_{D,rms}$ in CAV is higher than that in OA due to the strong flow unsteadiness occurred in CAV.

Fig. 3 presents the time averaged streamwise velocity $\overline{u}$ of both cases together with the streamlines. Symmetric boundary layer development about the chord is evident in OA (Fig. 3a). Same as observed in Olsman and Colonius' work [13], the flow separates at about half the chord length. On the contrary, the boundary layer development in CAV (Fig. 3b) is very different. A boundary layer of momentum thickness $\theta_o \approx 0.01W$ emanates from the cavity leading edge and is $\sim 30\%$ thinner than that obtained by Olsman and Colonius [13]. Such thin shear layer tends to run into self-sustained oscillation according to the linear stability theory [23]. The boundary layer then separates from the airfoil at the cavity and reattaches to the airfoil at $x \sim 0.42$. Near the airfoil trailing edge, unlike the two separation regions as in OA, only a separation region is observed at the lower airfoil surface in CAV. The streamlines there also show some flow at the airfoil trailing edge traveling from the upper surface to the lower surface before leaving the airfoil.

Inside the cavity, two counter-rotating recirculating regions of comparable sizes are evident (Fig. 3c). The boundary layer leaves the cavity leading edge, thickens gradually until it reaches

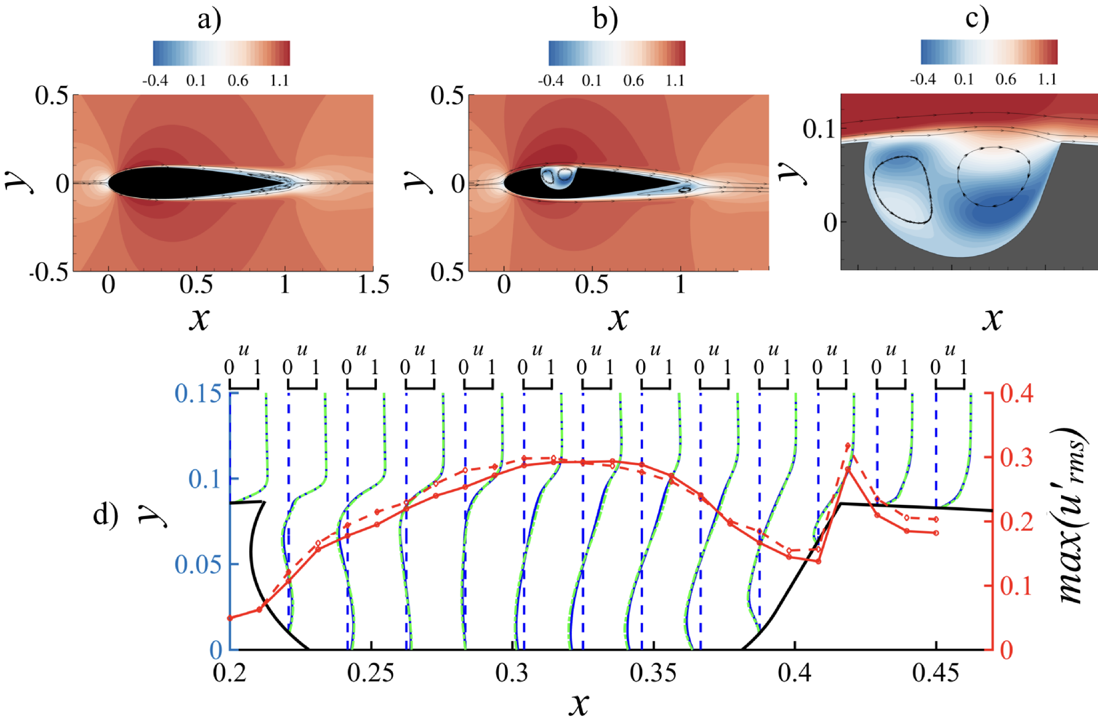

Fig. 3 Distribution of time averaged streamwise velocity $\overline{u}$ with streamlines. a) OA; b) CAV; c) close-up of cavity in CAV; d) selected profiles of $\overline{u}$ along the shear layer (blue - Mesh A; green - Mesh B) and variation of maximum u'_{rms} across cavity (red - Mesh A; red - - Mesh B) .

about one third of the cavity where its thickness jumps sharply. In particular the boundary layer thickness increases towards the interior of the cavity due to the entrainment of fluid near its opening via viscous momentum transport. Fig. 3d shows the evolution of $\overline{u}$ across the cavity obtained from Mesh A (blue solid line) and B (green solid line). The blue dashed line for $\overline{u} = 0$ marks the location where each $\overline{u}$ profile was extracted. The profiles of $\overline{u}$ from both meshes are very close. Furthermore, the maximum rms value of u' (u'_{rms}) on each profile is calculated and plotted in Fig. 3d. The u'_{rms} increases and reaches a plateau at $0.29 < x < 0.34$. Then it decreases until reaching the cavity trailing edge and shows a sudden jump again. Since the aerodynamic fluctuations from both meshes have insignificant differences, we will concentrate on the results from Mesh A in the forthcoming discussions of aerodynamics.

The distributions of u'_{rms} and v'_{rms} in OA (Figs. 4a and 4b) are symmetric about the chord and show high levels near the flow separation regions and the wake. Their magnitudes are much stronger

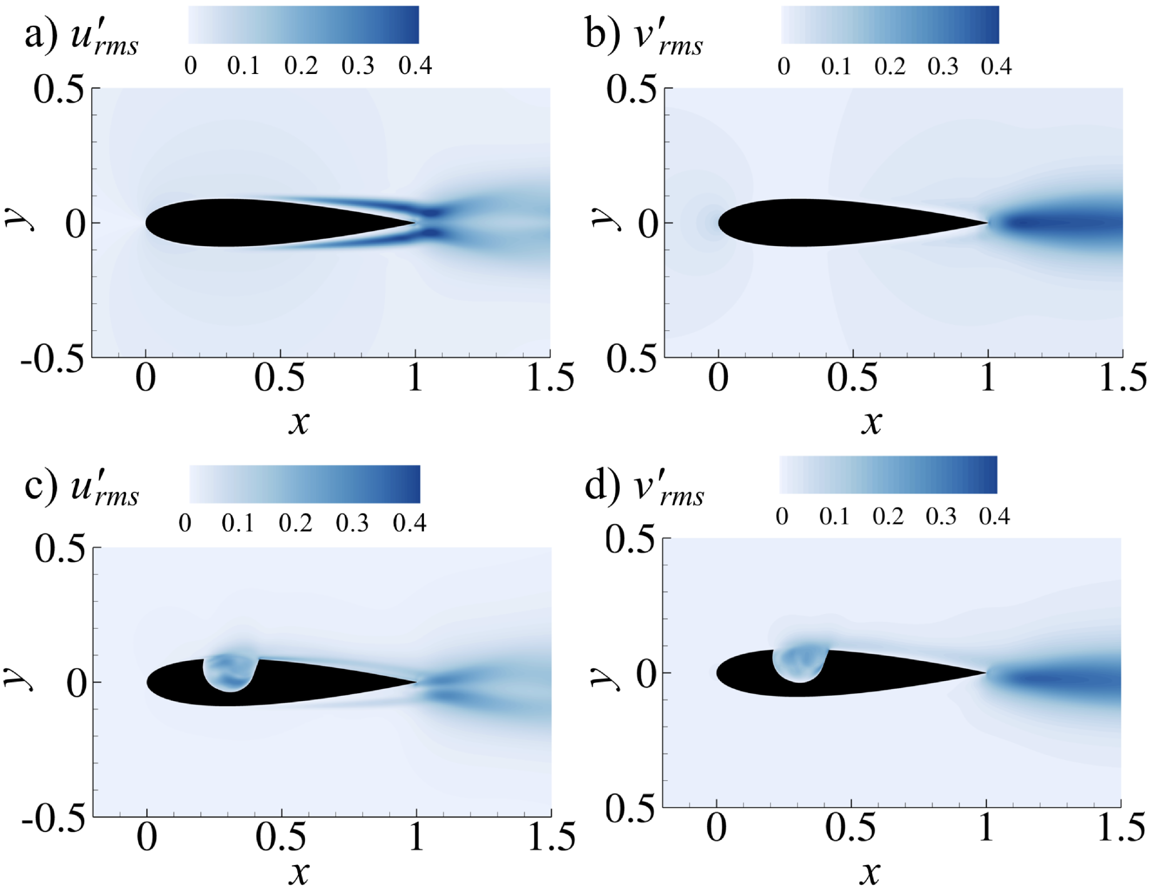

Fig. 4 Velocity fluctuations u'_{rms} and v'_{rms}. a) and b), OA; c) and d), CAV.

than those in CAV, suggesting much more intense aerodynamic fluctuations than those in CAV. In CAV, these two rms values show high levels in two regions inside the cavity (Figs. 4c and 4d). The first one is at the cavity bottom near downstream wall, which indicates vigorous flow unsteadiness due to the flow impingement there. The second one is at the opening of the cavity, especially near one third of the cavity where the shear layer thickens abruptly (Fig. 3d). After the flow passes the cavity, the velocity fluctuations weaken and concentrate within the boundary layer region. The fluctuation strengthens again in the wake region of the airfoil due to strong vortex shedding there.

B. Unsteady Airfoil Aerodynamics

Fig. 5 illustrates the unsteady flow dynamics in OA. The two boundary layers continue to grow after flow separation, roll up in the vicinity of the airfoil trailing edge and induce counter-rotating secondary vortices which create strong transverse flow fluctuation. Analysis of v' at probe B gives

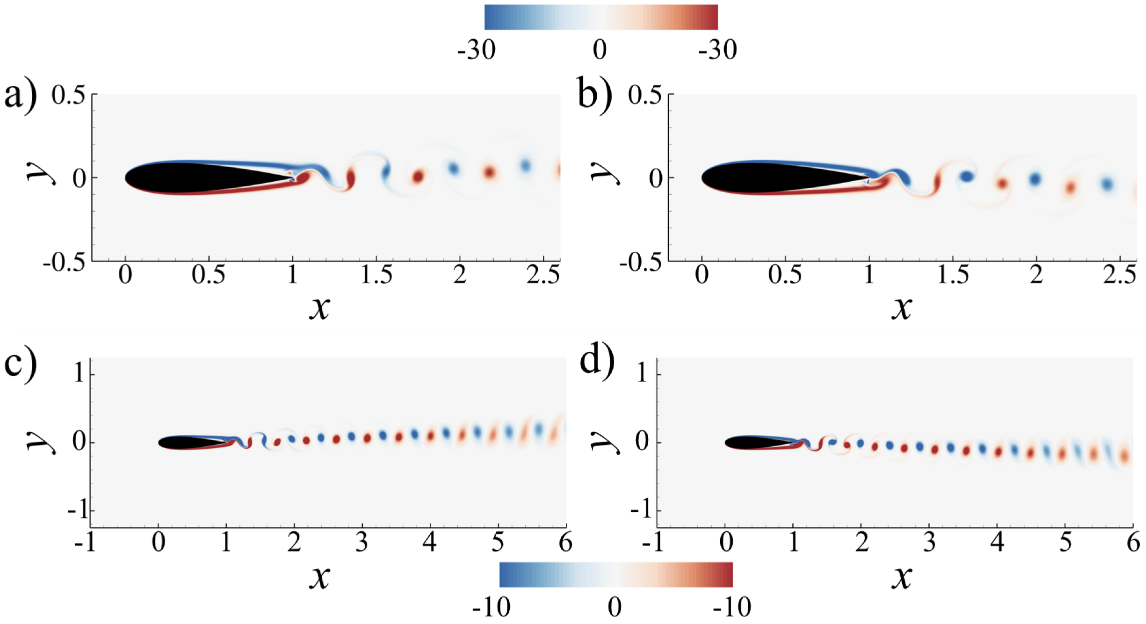

Fig. 5 Snapshots of vorticity distribution in OA. a) At $t = 120$; b) at $t = 130$; low frequency flapping of airfoil wake, c) At $t = 120$; d) at $t = 130$.

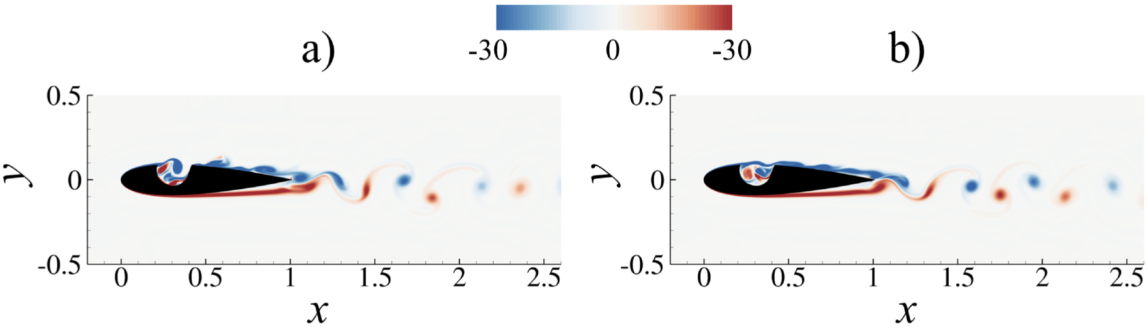

Fig. 6 Snapshots of vorticity distribution in CAV. a) First shear layer mode (Mode I); b) second shear layer mode (Mode II).

a Strouhal number $St_H = fH/U_\infty = 0.42$ (Table 2) which agrees well with those in Olsman and Colonius' work [13]. Furthermore, a low frequency flapping of the entire wake at $St_{H,LFO} \sim 0.01$ as observed in their work is present in OA results (Fig. 5c and d) in response to the oscillation of flow separation points. Olsman and Colonius found that the flapping is very sensitive to Re_∞, the airfoil profile and three dimensional effects. In CAV, no such low frequency flapping of the wake structures is observed.

Fig. 6 shows a complicated picture of the unsteady flow dynamics in CAV. The thin upper boundary layer oscillates as it leaves the cavity leading edge and induces a self-sustained oscillation according to linear stability theory [23]. Two observed dominant modes of oscillation are illustrated in this figure. In the first shear layer mode (Mode I), the boundary layer entrains a portion of free-stream fluid to form vortical structures that impinge the downstream wall of the cavity (Fig. 6a). The second shear layer mode (Mode II) however displays only a mild oscillation (Fig. 6b). The shear layer covers nearly the whole cavity and oscillates with a smaller amplitude than that of Mode I. Under the shear layer, two dominant vortical structures counter rotate inside the cavity. Switching between these two modes are noticed in the present results. Olsman and Colonius [13] also observed the same two modes as well as their switching in both their numerical calculations and experiments. However, the present Mode I appears to be less vigorous than that observed in their flow visualization, implying a milder interaction between the cavity shear layer and the cavity. As suggested by them [13], a possible cause of such difference is the modulation of the flow by three-dimensional instabilities of the recirculating flow in cavity and by the boundary layers at the spanwise end of the cavity. Further downstream of the airfoil, the shear layers roll up and shed vortices forming a vortex street.

Fig. 7 shows the time histories of calculated C_L and C_D. In OA, C_L exhibits periodic fluctuations at the frequency of vortex shedding near trailing edge superposed on the frequency of wake flapping. Conversely, C_L in CAV shows an irregular fluctuation with rich frequency contents. The major contribution to such high $C'_{L,rms}$ in OA (Fig. 7a) is the low frequency wake flapping whose amplitude is about 4 times larger than that induced by vortex shedding. The order of magnitude increase is comparable to that reported in the literature [13]. The wake flapping however does not create a strong fluctuation in C_D (Fig. 7b). In CAV, C_D fluctuates strongly as a result of intense flow unsteadiness generated by the cavity, which highlights the important role of cavity in generating the airfoil drag.

1. *Spectral and Time-Frequency Analyses*

In a flow past a cavity flush-mounted on an infinitely large flat surface, a shear layer emanating from the cavity leading edge impinges on the cavity trailing edge at which an acoustic wave is gen-

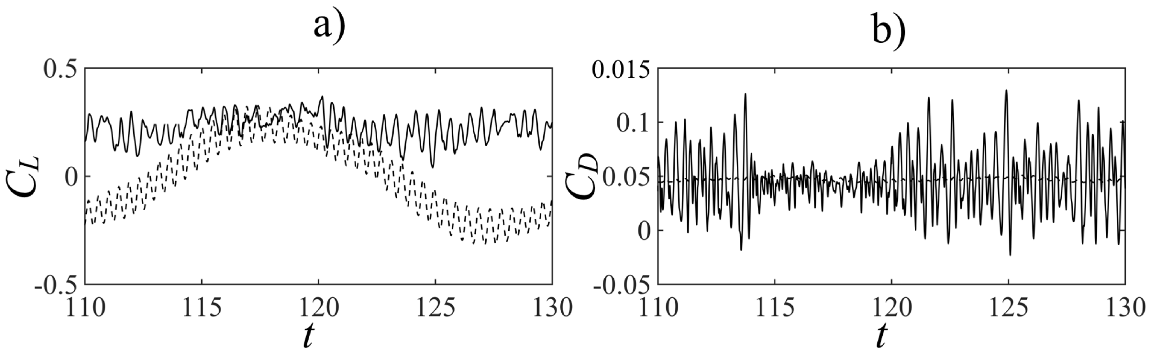

Fig. 7 Time histories of C_L and C_D. —, CAV; - - -, OA.

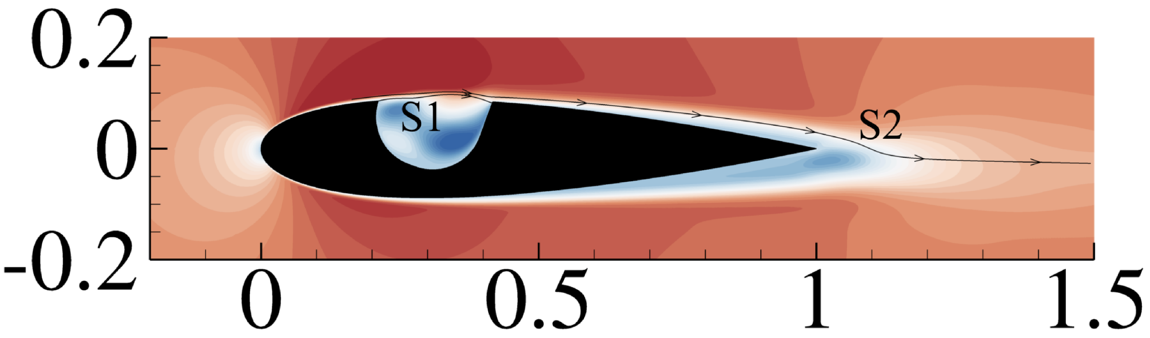

Fig. 8 The chosen streamlines S1 and S2.

erated and travels upstream. This in turn modifies the formation of the impinging shear layer. Such process leads to the occurrence of Rossiter mode [24], a spectacular self-sustained flow oscillation. It is informative to see if Rossiter modes exist in the present cavity in CAV. At low Mach number, the Strouhal number of the n-th Rossiter mode, based on cavity width W, may be estimated as [25]

$$St_{W,n} = \frac{n - \varphi}{1/\kappa + M_\infty / \sqrt{1 + (r_T/2)(\gamma - 1) M_\infty^2}}, \tag{2}$$

where r_T is the thermal recovery factor and is set to 1 for a low Mach number flow [25]. The quantity κ is the average convection speed of disturbances in the shear layer and its estimation follows the method suggested by Terracol et al. [26]. In essence, it takes the average of the convection speeds estimated from a 5-point correlation of pressure fluctuation at various locations along a streamline. A streamline covering the cavity (S1 in Fig. 8) is chosen and the corresponding κ is 0.588. The quantity φ is the phase delay which can be estimated as [27],

$$\varphi = -0.2125 + 0.13625\,(W/D) - 0.005625\,(W/D)^2\,. \tag{3}$$

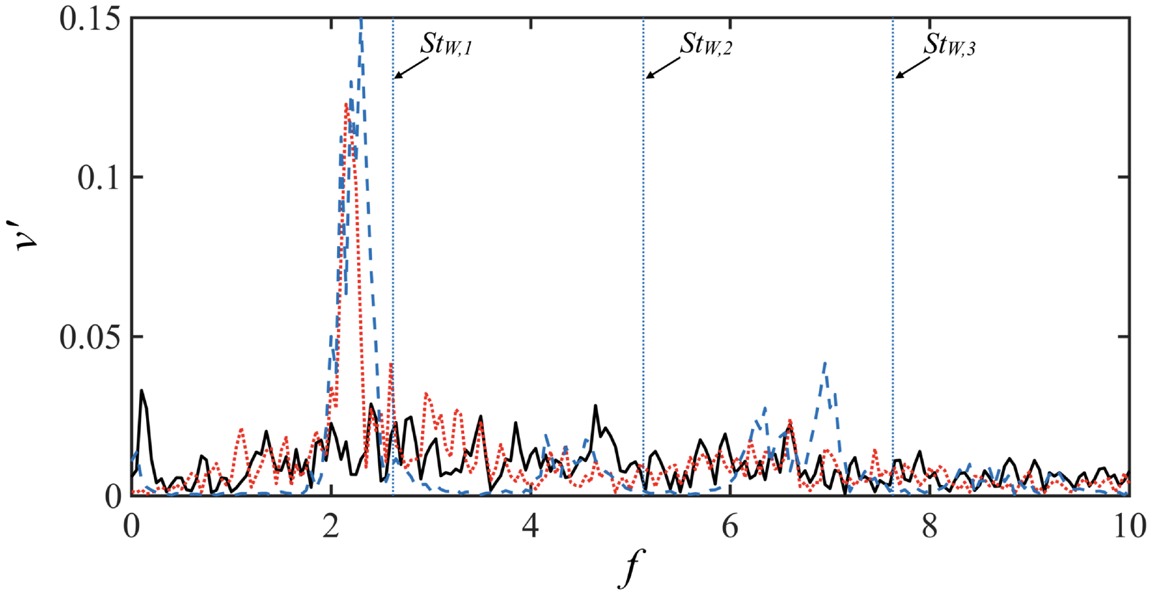

Fig. 9 Spectra of v'. Black —, probe A (CAV); red ···, probe B (CAV); blue - - -, probe B (OA).

In the present study, $W/D = 1.3$, so the first four estimated Rossiter modes $St_{W,1-4}$ are 2.62, 5.13, 7.63 and 10.14 respectively. Since $St_{W,1}$ and $St_{W,2}$ agree very well with Mode I and Mode II in the results of Olsman and Colonius [13] respectively, we expect Mode I and Mode II in the present calculation occurs at frequencies near these two St_W.

The velocity fluctuation v' at the probes A and B (Fig. 1) in both cases are processed with Hamming windowed Fast Fourier Transform (FFT) to obtain their spectra. The sampling frequency is 16000 and no overlapping of data is applied in the transform. In OA, the vortex shedding frequency at the airfoil trailing edge and its higher harmonics characterize the spectrum at probe B (Fig. 9). In CAV, the presence of cavity slightly reduces St_H to 0.39. In addition to the similar observations for the spectrum at probe B in OA, this spectrum exhibits rich contents in other frequency ranges as a result of vortex shedding from the cavity. However, its peak amplitude is about 15% smaller than that in OA. This suggests that even though the possesses in CAV complicates unsteady aerodynamics, the strength of the unsteadiness is actually weaker than that in OA. At probe A in CAV, many strong frequency components are present other than the vortex shedding frequency of the airfoil trailing edge $f_{v,CAV,0} = 2.15$. Our calculated Mode I is very close to $ST_{W,1}$, which is slightly higher than the prediction using Eq. (2) by $\sim 0.4\%$. Near other Rossiter mode frequencies, only weak components are observed. Generally, the flow dynamics at the cavity and its generated acoustics do not align sufficiently to create a strong Rossiter mode in this case. All other strong peaks in Fig. 9 may be caused by the vortex shedding in the vicinity of the cavity leading edge or other flow dynamics. Furthermore, the frequencies of flow dynamics inside the cavity and the airfoil trailing edge are quite close.

In order to understand the mode switching better, we performed a time-frequency analysis. Since the switching dynamics is not known priori, wavelet analysis is a good choice for its little compromise between the time resolution and frequency resolution [28]. In essence, it involves a convolution of a temporal data and an arbitrary wavelet time function, which possesses a wavelet scale s as a measure of its period. By selecting a scale in the convolution, one can obtain the strength of the data in that particular scale. In the present study, the complex Morlet wavelet function Ψ is adopted for its popularity in fluid dynamics. It is expressed as

$$\Psi\left(\eta\right) = \pi^{-1/4} e^{i\omega_o \eta} e^{-\eta^2/2}, \tag{4}$$

where $i = \sqrt{-1}$, η is a time parameter related to the sampling frequency, the scale s and total length of the data, ω_o is the central frequency set to 6 for satisfying the admissible condition [29]. The scale of this wavelet is defined as the peak to peak duration. The procedure of the wavelet analysis mainly follows Torrence and Compo [28], except the final normalization of the results to have unity energy for each wavelet scale. As such, the amplitude of different scales can be compared directly. In the present study, 20000 uniform intervals are used in the scales corresponding to the interested range of frequency between 0.01 and 10. Zero padding is applied to the data so that the total length of the data is increased to the next higher power of 2.

Fig. 10 illustrates a comparison of magnitude of v' wavelet spectra at probe B. The black solid lines in the figure show the loci of the maximum amplitude. The red dashed lines denote the boundaries of a zone called cone of influence below which the results are ignored due to the excessive influence of zero padding. In OA, the vortex shedding frequency at the trailing edge $f_{v,\mathrm{OA},0} = 2.35$ dominates the wavelet spectrum throughout the analyzed period (Fig. 10a). Occasionally, its first harmonic $f_{v,\mathrm{OA},1} = 4.70$ and its second harmonic $f_{v,\mathrm{OA},2} = 6.95$ also appear. The wake flapping frequency cannot be observed because it lies in the cone of influence. However, $f_{v,\mathrm{OA},0} = 2.35$ slightly

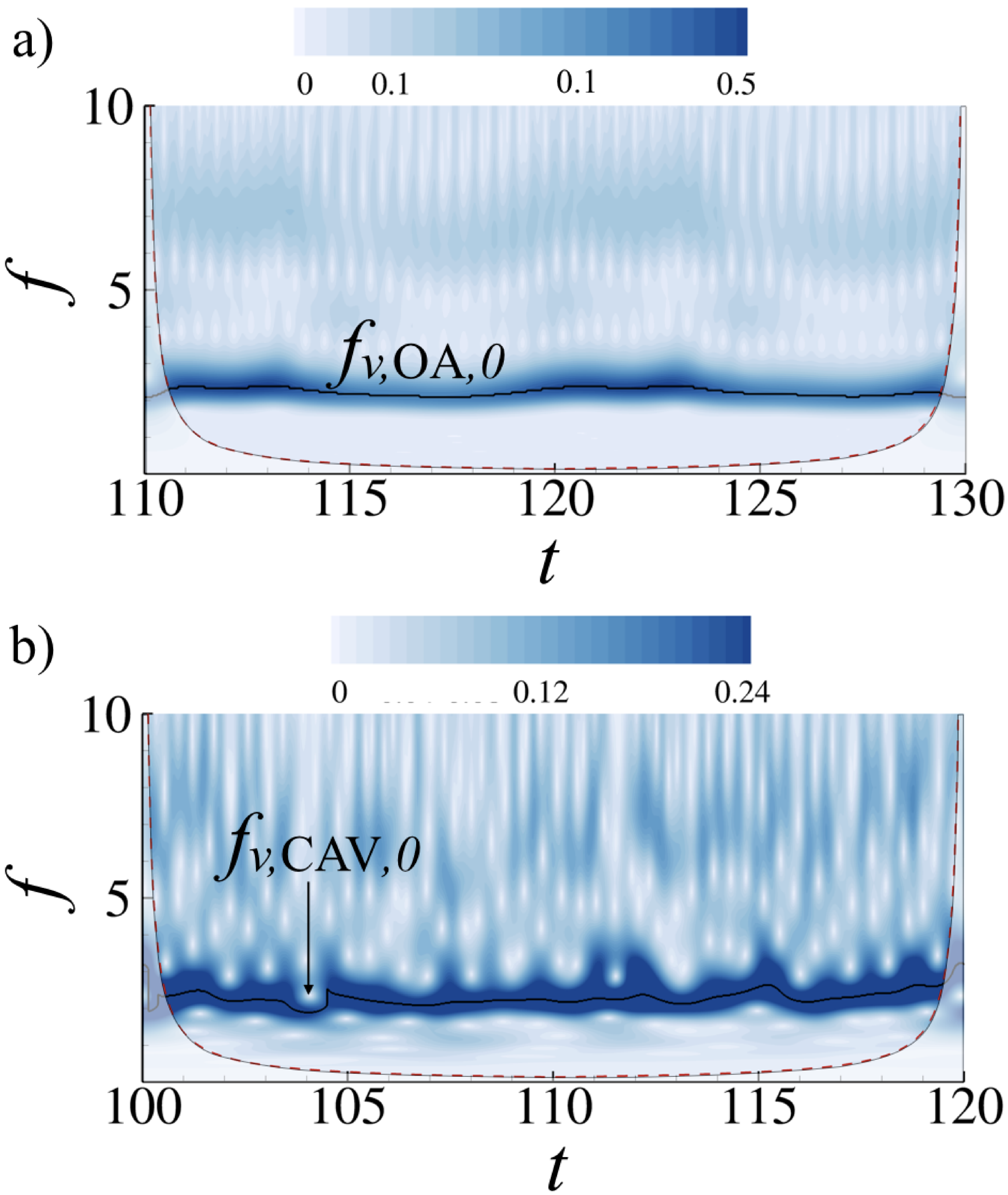

Fig. 10 Magnitude of v' wavelet spectra at probe B. a) OA; b) CAV.

modulates at a frequency doubling that of wake flapping. This modulation may be caused by the wake flapping. The dominance of all the reported frequencies gives further support to the previous argument that the vortex shedding and wake flapping are the major unsteadiness in OA. On the contrary, in CAV, v' fluctuates near $f_{v,,\mathrm{CAV},0} = 2.15$ within frequency range $1.95 < f < 2.55$. The

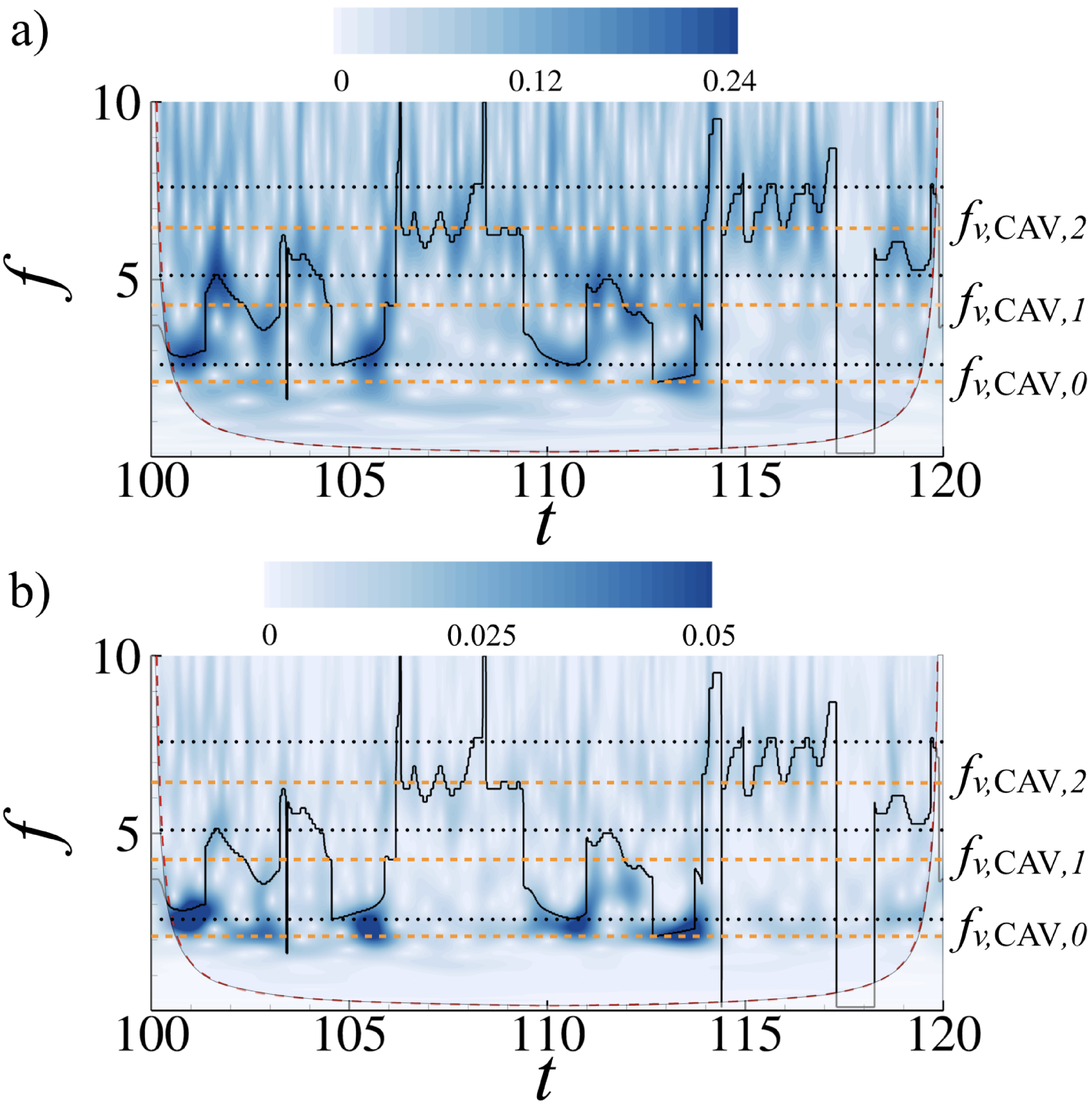

Fig. 11 Wavelet results of v' in CAV. a) Magnitude of wavelet spectrum at probe A; b) magnitude of cross wavelet spectrum between probe A & probe B, W_{AB}; $\cdots$, $St_{W,n}$, $n = 1 - 3$.

frequency modulates irregularly over time possibly as a result of irregular vortex shedding from cavity flow, which gives rise to a jittering effect that is commonly observed in flow past cavities [30, 31]. Unlike in OA, no prolonged harmonics of the vortex shedding frequency is observed. Instead, the wavelet result shows intermittent strong fluctuations at frequencies higher than $f_{v,\text{CAV},0}$. All these observations evidently highlight the key role of unsteady cavity flow and prompt for a wavelet analysis inside the cavity.

Fig. 11a illustrates the magnitude of v' at probe A inside the cavity in CAV. A rapid mode switching in the analyzed is clearly observed. The mode switching in general does not follow a specific pattern and is not limited to $St_{W,1}$ and $St_{W,2}$. Instead, in most of the time v fluctuates at frequencies other than the estimated Rossiter modes. These frequencies include the vortex shedding frequency at the airfoil trailing edge and its harmonics. This supports the previous finding that Rossiter modes are not the dominant flow dynamics in the present case. Furthermore, there are still some unidentified frequencies with high level of fluctuations such as those during $t = 102 - 104.5$. This implies that in addition to the shear layer modes and vortex shedding near the airfoil trailing edge, the flow inside cavity are under the influence of some other flow dynamics.

To further explore the relationship between these unidentified flow dynamics, the cross wavelet spectrum W_{AB} of v' at both probes A and B may help provide an insight. It is defined as the product of the wavelet spectrum of probe A and the complex conjugate spectrum of probe B (denoted by *), i.e. $W_{AB} = W_A W_B^*$. Fig. 11b shows the cross wavelet spectrum W_{AB}. The region with the highest level of fluctuation lies mainly between $f_{v,\mathrm{CAV},0}$ and that of $St_{W,1}$ due to the strong fluctuations of the vortex shedding near airfoil trailing edge and Mode I. One should note that along the locus of the maximum amplitude, W_{AB} shows a rather high value (> 0.01). This implies that the velocity fluctuations between the cavity and the airfoil trailing edge are connected to certain extents. Thus, these unidentified flow dynamics may be related to the interactions between these flow dynamics of the cavity and the airfoil trailing edge. Furthermore, some regions outside this locus also show quite high values of W_{AB}. This suggests the concurrency of various flow dynamics occurred in the airfoil with cavity, which makes the aerodynamics in CAV is much more complicated than those of single airfoil or cavity alone. In addition, we also inspected the phase of W_{AB}. This, however, is not shown here because it is quite erratic to deduce any clear relationship between various flow dynamics further.

C. Acoustic Generation

Fig. 12 shows the instantaneous acoustic pressure p' in both cases. In OA, acoustic waves appear to originate from the airfoil trailing edge and display a regular symmetric pattern about the airfoil chord (Fig. 12a). The strongest radiation goes along $\theta = \pm 120^\circ$ but the weakest radiation

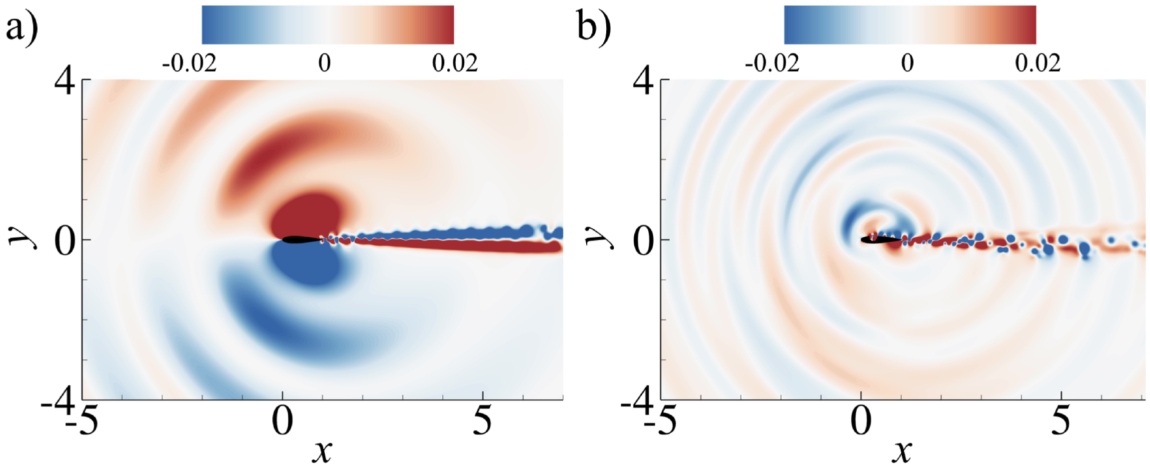

Fig. 12 Instantaneous acoustic fluctuation p'. a) OA; b) CAV.

resides airfoil upstream at $\theta = \pm 175°$. In CAV (Fig. 12b), acoustic waves appear to be generated from both cavity and airfoil trailing edge, resulting in a complex asymmetric radiation pattern. Fig. 13 illustrates the time traces of p' at selected locations in far field. In general, the vortex shedding and wake flapping frequencies prevail in p' in OA forming a tonal nature of the radiation. In CAV, p' exhibits irregular fluctuations and contains much more frequency content. Furthermore, its fluctuating amplitude appears to be smaller that in OA.

Fig. 14 illustrates the directivity of p'_{rms}, calculated from p' of the whole analyzed period, i.e. $T = 20$, along the radius $r = 3.5$ from the airfoil trailing edge. In both cases, the strong aerodynamic fluctuations inside airfoil wake (i.e. $\theta = \pm 10°$) dominate to mask out the acoustic fluctuations (Fig. 12); thus, the data in this sector is not shown. The figure clearly demonstrates the strong influence of cavity on the acoustic directivity. Clearly the acoustic generation in OA is symmetric. It exhibits a strong preference along $\theta = 120°$ but radiates the weakest along $\theta = 180°$. The acoustic generation in CAV loses the symmetry completely and shows a strong generation from the upper airfoil surface with its peak along $\theta = 135°$. The most remarkable feature in this figure is that the flow in CAV generates weaker acoustic waves consistently than that in OA in nearly all θs. The acoustic reduction is much more prominent in the region below the airfoil. The maximum reduction is about 3.1 dB ($\theta = 88.0°$) and 3.9 dB ($\theta = 265.3°$) in the upper and lower domains respectively. Such observation is rather insensitive to the mesh design. Hence, the results calculated

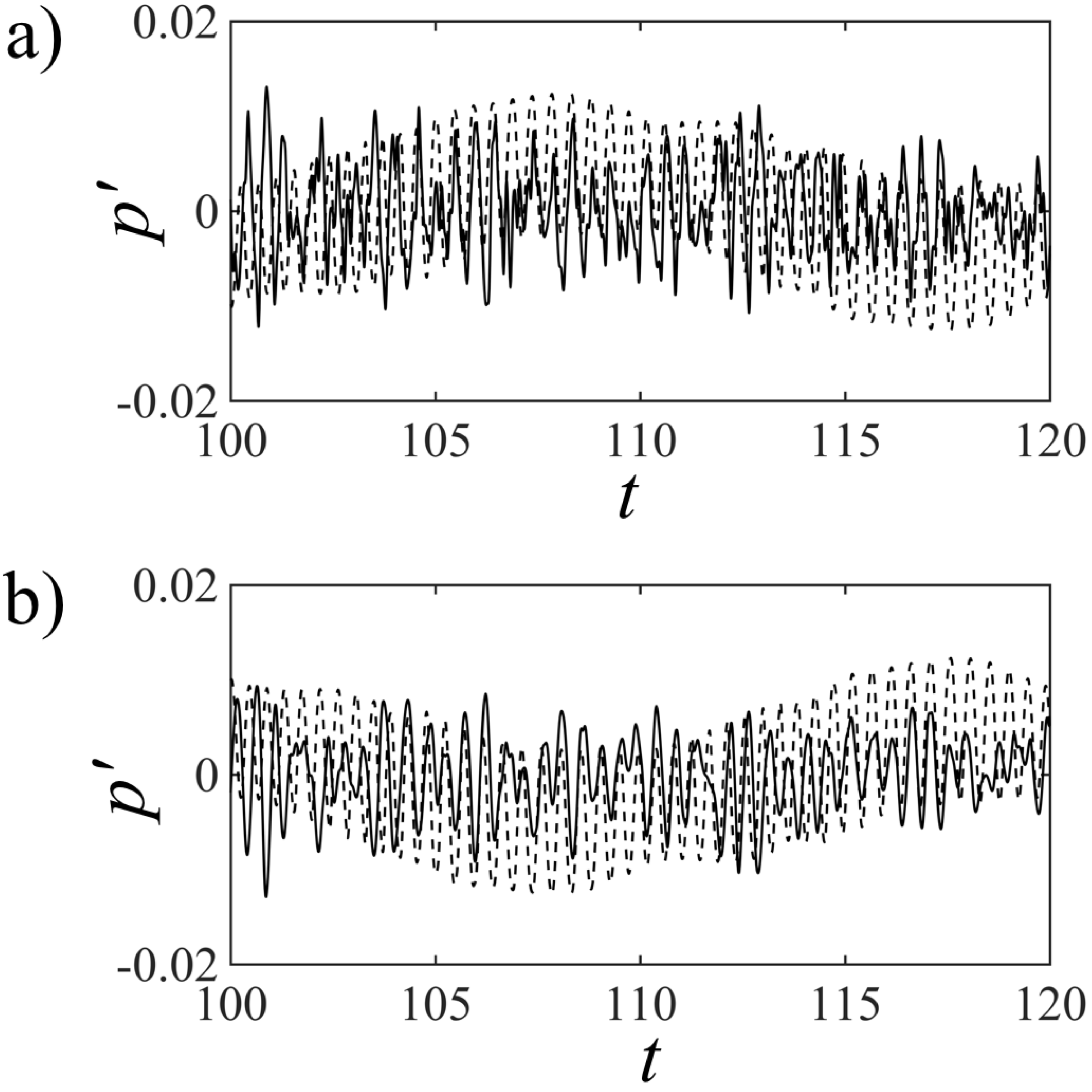

Fig. 13 Time traces of acoustic pressure p'. a) At $(1.0, 3.5)$; b) at $(1.0, -3.5)$. —, CAV; - - -, OA.

with Mesh A are concentrated in the forthcoming analyses.

In the previous section, the observed low frequency wake flapping is similar to that observed by Olsman and Colonius [13] who claim that such flow feature is triggered with particular combinations of airfoil profile and flow condition. It is not clear if the present problem setting hits one of their said combinations. As there is no wake flapping in CAV results, it is interesting to compare the acoustics of two cases when excluding the contribution of wake flapping in OA. Therefore, we included the p'_{rms} obtained from high-pass filtered p' time trace in OA in Fig. 14 for comparison. The strength of filtered p'_{rms} from the upper airfoil surface now decreases to be comparable to that in CAV. The

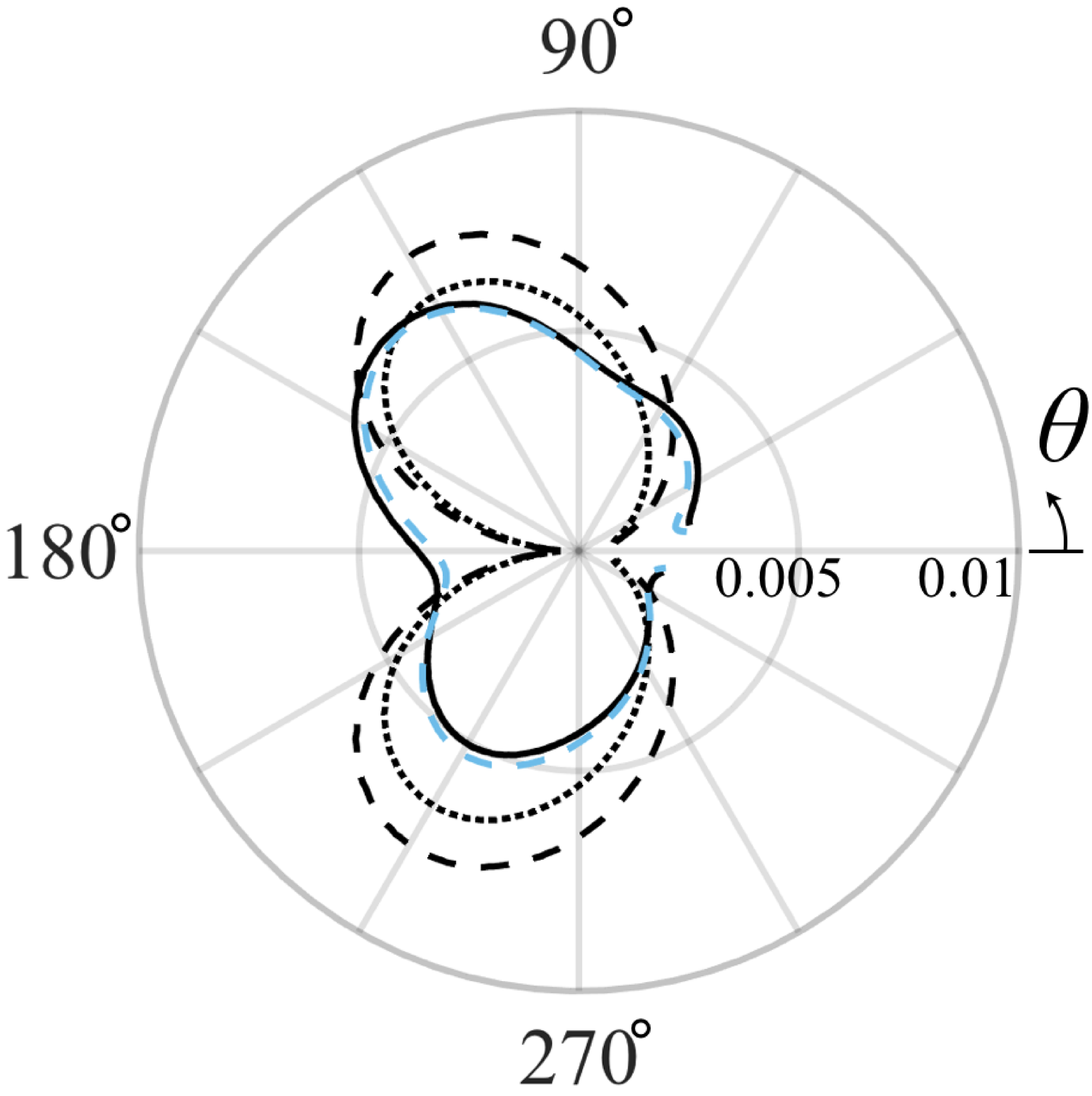

Fig. 14 Directivity of p'_{rms} at $r = 3.5$ measured from airfoil trailing edge. Black —, CAV (Mesh A); blue - - -, CAV (Mesh B); black - - -, OA; $\cdots$, OA filtered.

change clearly confirms the large acoustic contribution of the wake flapping in OA. Nevertheless, the acoustic generation from the lower airfoil surface in CAV is still much weaker than that in OA. The maximum reduction now is about 1.4 dB ($\theta = 91.0°$) and 2.4 dB ($\theta = 253.8°$) from the upper and lower airfoil surfaces respectively. The reduction clearly reveals the high potential of introducing cavity flow for airfoil aeroacoustics control.

We further estimated the acoustic intensity through $r = 3.5$ using the expression given in Lam et al. [16] for both cases, and then integrated the results to estimate their overall acoustic power

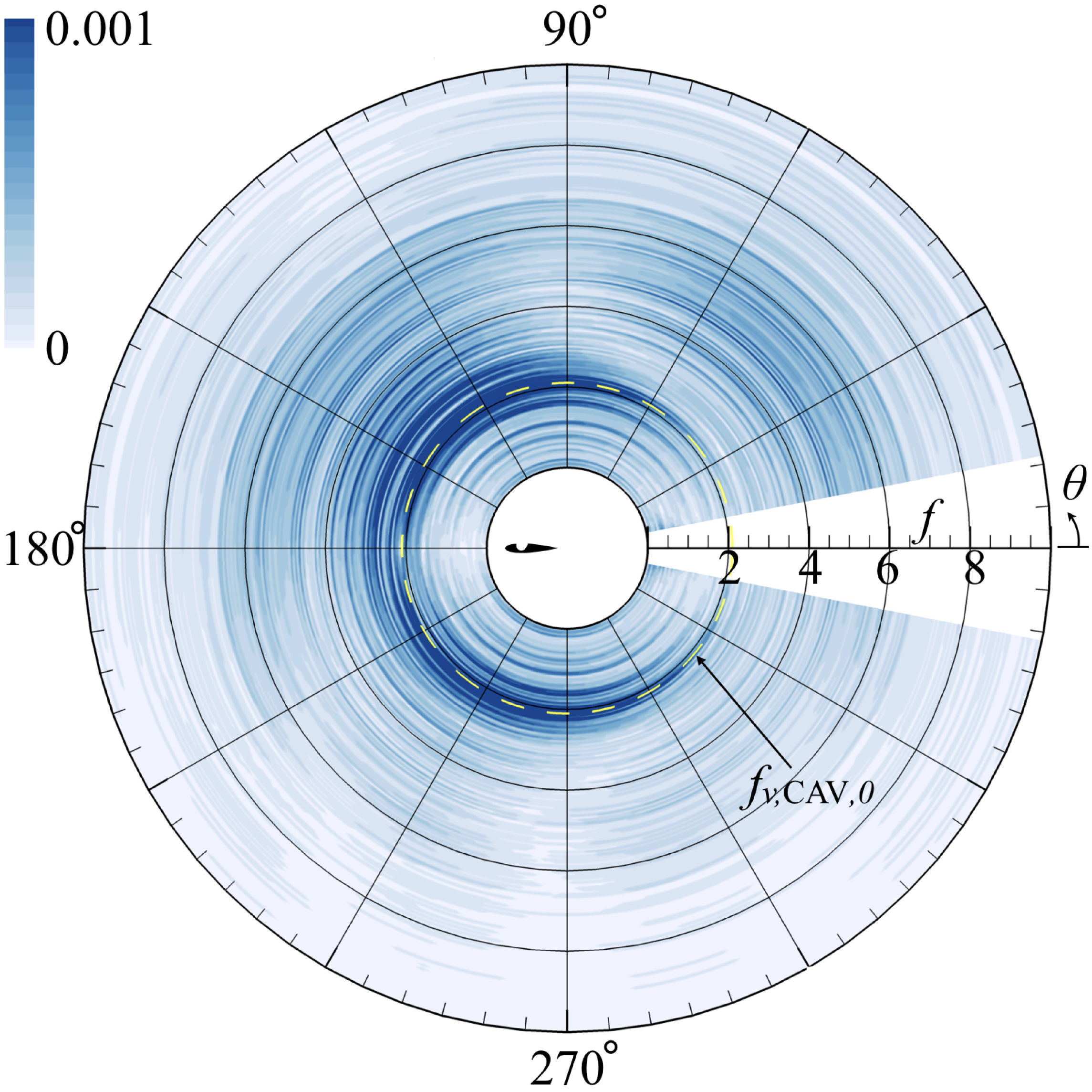

Fig. 15 Directivity of p' spectrum at $r = 3.5$ for CAV.

for comparison. The contribution of wake flapping is filtered out so that the comparison presents a conservative scenario. It is found that the presence of the cavity effectively reduces the acoustic power radiation by 1.2 dB and 2.6 dB from the airfoil upper and lower surfaces respectively.

To gain further insight of the acoustics in CAV, FFT of p' time traces at all θs on $r = 3.5$ was performed to obtain the acoustic spectral directivity (Fig. 15). All the data was obtained with a sampling frequency 16000 unless specified otherwise. Hamming window is also applied to p' without any data overlapping. The yellow dashed line marks the vortex shedding frequency $f_{v,\mathrm{CAV},0}$ at the airfoil trailing edge. In summary, the acoustic generation in the low frequency range ($f < 2$) is

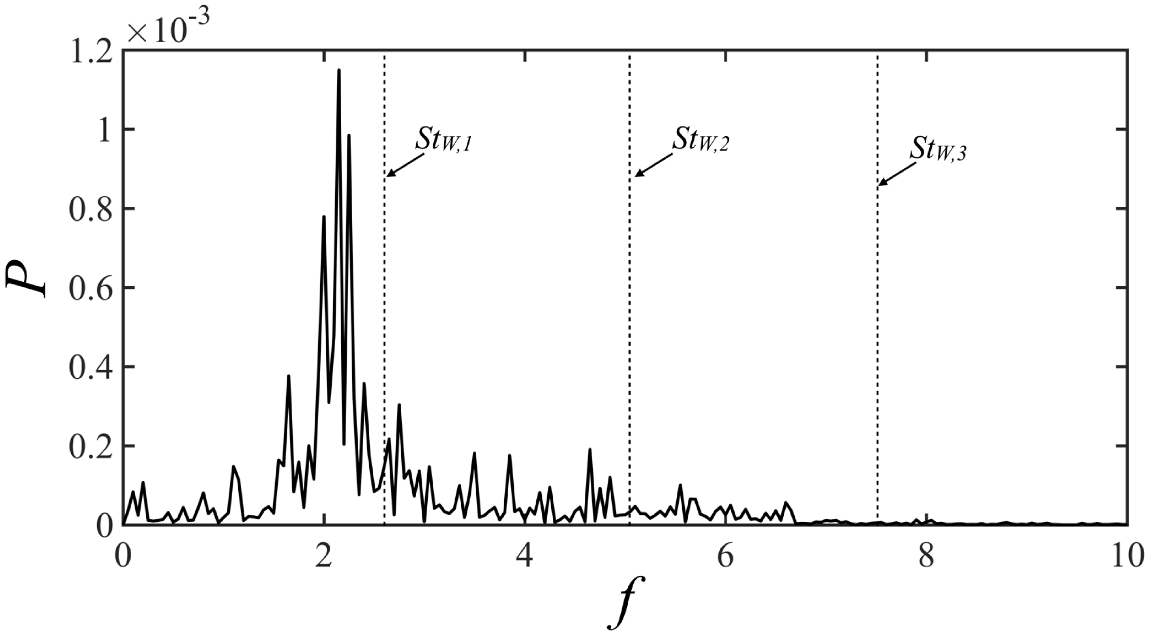

Fig. 16 Spectrum of power P for CAV.

weak in all directions. The strongest contribution comes from mid-range frequencies ($2 \leqslant f \leqslant 4$) which then decreases as f further increases. At very high frequencies, the acoustic contribution from this zone in all directions is very small. The spectral content of the generated acoustic wave varies with θ too. The second quadrant contains the strongest and richest spectral content in both mid-range $2 \leqslant f \leqslant 4$ and high frequency range $4 \leqslant f \leqslant 7$. The situation in the third quadrant looks similar but the generation in high frequency range is less prominent. The fourth quadrant is comparatively quiet with contribution from $2 \leqslant f \leqslant 4$. Fig. 16 gives the overall signal FFT spectral power P estimated by summing the square of individual p' spectrum in Fig. 15. There are prominent contributions concentrated around the frequency $f_{v,\mathrm{CAV},0} = 2.15$ of vortex shedding amid other peaks within $1.5 \leqslant f \leqslant 6.7$. This observation suggests that the vortex shedding from the airfoil trailing edge is still the dominant acoustic generation process even in the presence of the cavity. However, all the acoustic generating flow dynamics in CAV occur at narrow range of frequencies and poses a great difficulty in differentiating them.

To attempt the differentiation of these flow dynamics we performed coherence analysis between p' at $(r, \theta) = (3.5, 135°)$ and the airfoil flow dynamics for CAV. v' along streamline S2 inside the boundary layer in Fig. 8 were chosen. In the analysis, the data was divided into 10 segments for

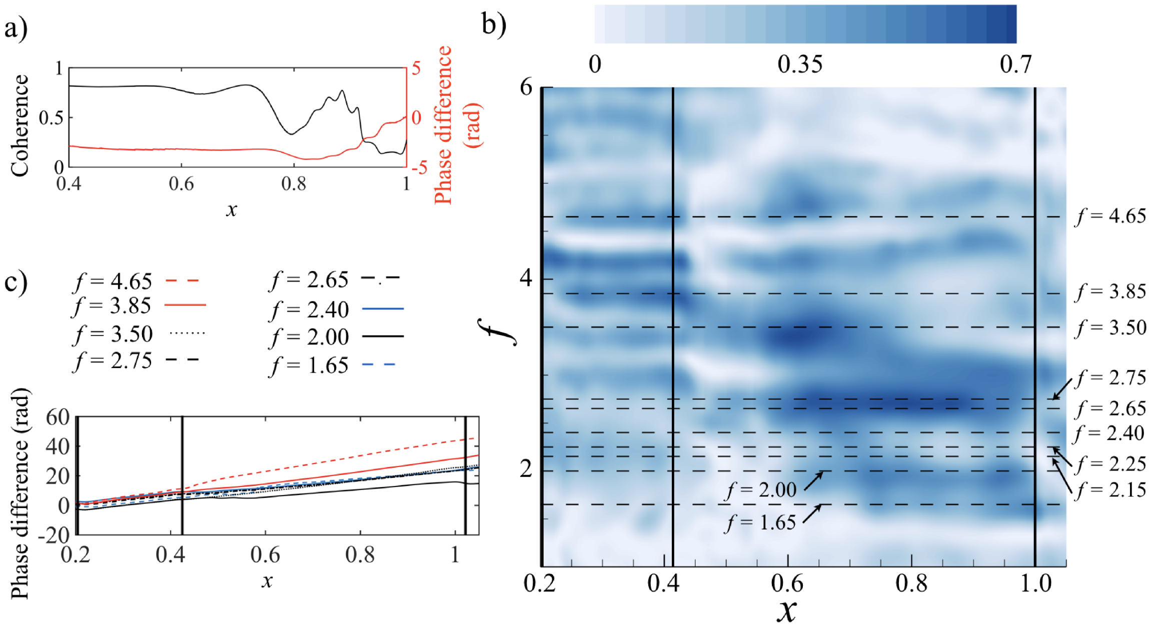

Fig. 17 Coherence between acoustic pressure p' at $(r, \theta) = (3.5, 135^{\circ})$ and velocity fluctuation v'. a) Magnitude and its phase difference at $f_{v,\mathrm{OA},0}$ in OA; b) Spectral map along streamline S2 in CAV; c) Phase difference of their cross spectra at dominant frequencies along streamline S2 in CAV.

data overlapping and the sampling frequency was set to 500. For comparison, coherence analysis is also performed for OA with using a streamline similar to S2 in Fig. 8 inside the boundary layer.

Fig. 17a shows the coherence at $f_{v,\mathrm{OA},0}$ between p' and v' along the chosen streamline. The phase difference of their cross spectrum is also plotted in this figure. Very strong coherence (> 0.8) is observed along the boundary layer except a dip near $x = 0.8$ where the flow separates from airfoil surface (Fig. 5). Meanwhile, the phase difference decreases in the upstream region but starts to increase at $x > 0.8$. These features signify a change in the flow dynamics at $x > 0.8$ probably due to the secondary vortices created in the vicinity of the airfoil trailing edge. The slope of the phase difference was also used to calculate the disturbance convective speed by following Schumacher et al. [14]. A phase difference of 2π indicates a traversal over one disturbance wavelength. Thus, the number of wave for convective disturbances can be estimated from the slope of this figure. The disturbance convective speed calculated at $x < 0.75$ is close to the negative speed of sound. Therefore, the disturbance traveling in this region is mostly acoustic. Convective flow disturbances propagating downstream were not found in this region. Thus, it is very likely that vortex shedding at airfoil trailing edge, rather than feedback mechanism, creates the airfoil tones in this case.

Fig. 17b illustrates the distribution of coherence spectrum along S2 in CAV. The vertical lines indicate the cavity edges and the airfoil trailing edge. The horizontal lines mark the dominant frequencies with power $P > 1.8 \times 10^{-4}$ in Fig. 16. In general, strong coherence is found along the boundary layer between the cavity trailing edge and airfoil trailing edge ($0.42 < x < 1$). The coherence at the cavity shear layer is slightly weaker than that in its downstream region. It is possibly caused by the frequent mode switching occurred in cavity flow (Fig. 11). This sets to make the acoustic generation by the cavity less effective. At $f = 3.85$ and 4.65, the coherence along the cavity shear layer is higher than that along the boundary layer downstream. This implies that these two tones are possibly generated by the cavity flow dynamics alone. At frequencies $f = 2.15$, and 2.25, the overall coherences are rather weak in the whole range of x but increase towards the downstream of airfoil trailing edge. This suggests that the two major tones from airfoil trailing edge may not be attributed to a feedback mechanism, which should give a rather strong coherence along the boundary layer. Finally, other dominant frequencies show strong coherence along the boundary layer.

Schumacher et al. [14] argue that the multiple tones observed in their experiments are more likely to be generated by a feedback mechanism rather than vortex shedding at single frequency. Their results illustrate that the coupling between the convective boundary layer disturbances and the acoustic disturbances from airfoil trailing edge creates an aeroacoustic feedback loop responsible for the eventual airfoil tonal radiation. The frequencies of the feedback loop measured in their experiments agree favorably with the estimation proposed by Arbey and Bataille [32] , which reads

$$f_n = \frac{(n + 1/2)\, v_c}{L_d \left[1 + v_c / \left(c - U_\infty\right)\right]}, \tag{5}$$

where f_n is the frequency of the nth mode, L_d is the distance of the flow disturbances traveling in the feedback loop, v_c is the disturbance convective speed and c is the acoustic speed. In the present case, we take L_d as the distance between the cavity trailing edge and the airfoil trailing edge. The estimation of v_c was modified slightly to accommodate the multiple tones found in CAV. From the phase difference of the cross spectrum between p' and v' along streamline S2 (Fig. 17c), the disturbance convective speeds were calculated for the dominant frequencies. Then taking an average of these disturbance convective velocities, v_c was estimated to be 0.525. Then the estimated frequencies for modes 3 to 5 are 1.97, 2.75 and 3.54 respectively. These values are very close to some of the present dominant frequencies 2, 2.75 and 3.50 in the spectral power P (Fig. 16). If the distance between the cavity leading edge to the airfoil trailing edge is taken as L_d and same v_c is applied, the prediction yields 1.46, 2.04, 2.63 and 3.21 for modes 2 to 5 respectively. However, the difference between this prediction and the dominant frequencies increases and thus it is not likely that the feedback mechanism involves the cavity leading edge.

In order to get a clearer picture of underlying acoustic generating aerodynamics and further confirm the prediction of feedback mechanism, we performed FFT and filtered p' and v' fields of results in CAV at the dominant peaks. This analysis essentially adopted 10000 snapshots with equal time interval for a duration of 20 corresponding to about 30 cycles of the lowest frequency of interest. Fig. 18 to Fig. 20 illustrate the reconstructed solutions at selected frequencies. In these figures, the left and middle two columns are the snapshots of p' and v' respectively at the same time moment whereas the right column is the distribution of normalized fluctuation magnitude $|v'|/|v'|_{max}$, where $|v'|_{max}$ is the maximum $|v'|$ in the domain at each frequency. Although it is difficult to identify the acoustic generation at some frequencies even using this method, e.g. $f = 1.65$ and 2.4, we can identify three possible mechanisms of the acoustic generation from the interpretation of these results together with the previous coherence analysis.

Type I mechanism mainly concerns the acoustic generation at $f = 2.15$ and $f = 2.25$ (Fig. 18), which are the two most dominant contributors in the acoustic power (Fig. 16). They appear to originate from the airfoil trailing edge and share similar symmetric acoustic radiation to that in OA (Fig. 12a). The strongest radiation occurs at about $\theta = \pm 120^\circ$ and there is a silent zone near $\theta = 180^\circ$. A slight phase shift occurs between the radiation from the upper and lower airfoil surfaces. The exceptionally strong $|v'|/|v'|_{max}$ in the airfoil wake region provide a clear evidence for vortex shedding as the key acoustic generation process at these frequencies. Nevertheless, unlike the single vortex shedding frequency occurred in OA, the presence of cavity may promote jittering effect and the vortex shedding at the airfoil trailing edge results in two very close frequencies.

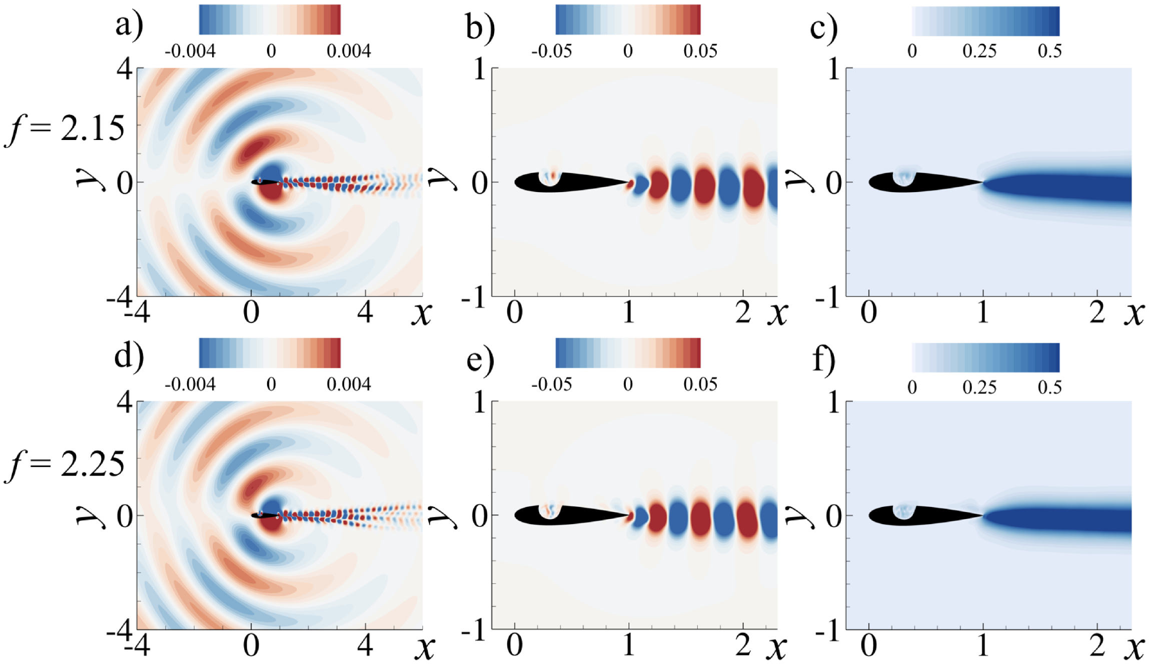

Fig. 18 Type I acoustic generation in CAV. a) - c) Instantaneous p', instantaneous v' and $|v'|/|v'|_{max}$ at $f = 2.15$; d) - f) instantaneous p', instantaneous v' and $|v'|/|v'|_{max}$ at $f = 2.25$.

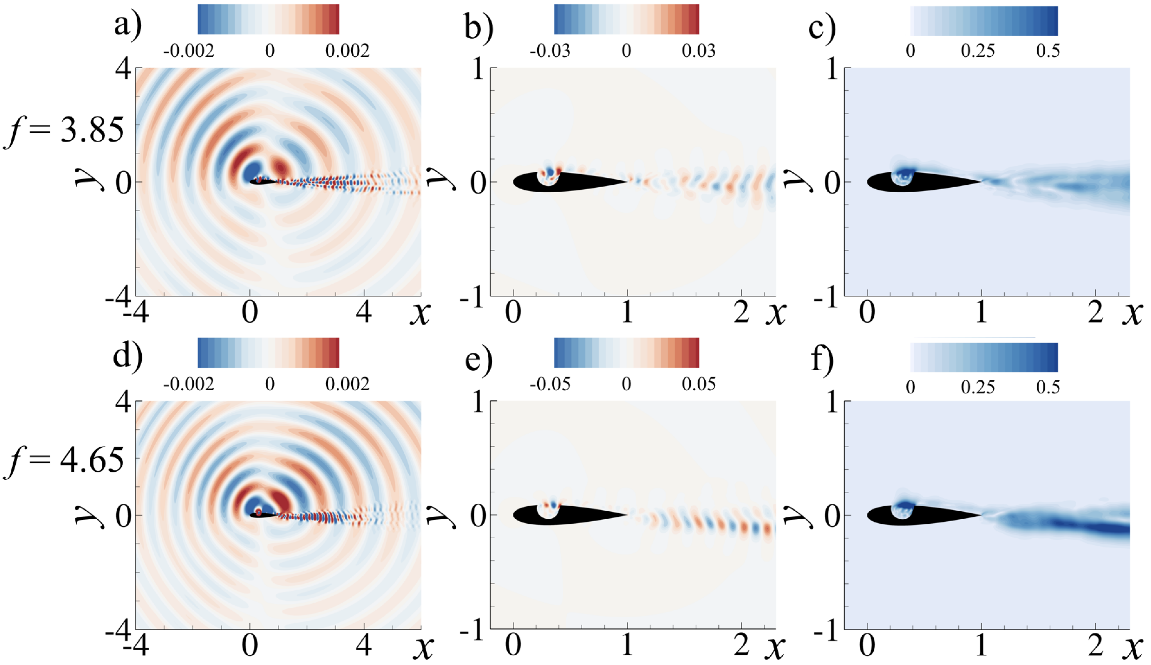

Fig. 19 Type II acoustic generation in CAV. a) - c) Instantaneous p', instantaneous v' and $|v'|/|v'|_{max}$ at$f = 3.85$; d) - f) instantaneous p', instantaneous v' and $|v'|/|v'|_{max}$ at$f = 4.65$.

The shear layer oscillation over the cavity is found responsible for the Type II mechanism. This shear layer mode is not limited to the Rossiter modes, but also the vortex shedding of the shear layer and their impingement on the cavity trailing edge like those at $f = 3.85$ and 4.65 in Fig. 19. Highly asymmetric acoustic radiation originates from the cavity trailing edge in the form of a streamwise dipole. It is generated by the impingement of vortices shed from the cavity leading edge on the cavity trailing edge. The acoustic wave propagate predominantly along $\theta = 45^\circ$ and 135° and are then scattered at the airfoil leading and trailing edges, creating two quiet directions along $\theta = 90^\circ$ and 270°. In addition, Fig. 19c and f clearly show strong velocity fluctuation in the cavity shear layer. This explains the strong coherence between the far field acoustics and cavity shear layer as shown in Fig. 17 at these two frequencies.

Type III mechanism involves three frequencies at which p' exhibit a preferential radiation along $\theta \approx 135^\circ$ (Fig. 20). The silent zones vary from 20° to 80° as the frequency increases. Scattering at both airfoil leading and trailing edges are also observed which become increasingly prominent as the frequency increases. The acoustic generation also seems to originate from the cavity. In addition, $|v'| \,/\, |v'|_{max}$ at all these frequencies shows strong levels in all boundary layer regions extending from the cavity to the airfoil wake. This is consistent with the strong coherence found along the boundary layer downstream of the cavity in Fig. 17. Their coherences also possess continuous phase differences from the cavity trailing edge to the airfoil trailing edge in Fig. 17c, supporting the occurrence of an acoustic feedback loop. Furthermore, these three frequencies also match closely the prediction using Arbey and Bataille's equation. Therefore, it is believed that Type III acoustic generation resembles in nature the aeroacoustic feedback loop between the cavity trailing edge and the airfoil trailing edge.

IV. Conclusions

The aeroacoustics of NACA 0018 airfoil with and without a cavity, respectively, were investigated numerically for zero angle of attack and compared with each other. The Reynolds number based on the chord length is fixed at 2×10^4. In general, the presence of the cavity completely modifies the unsteady laminar aerodynamics and the associated noise generation processes of the

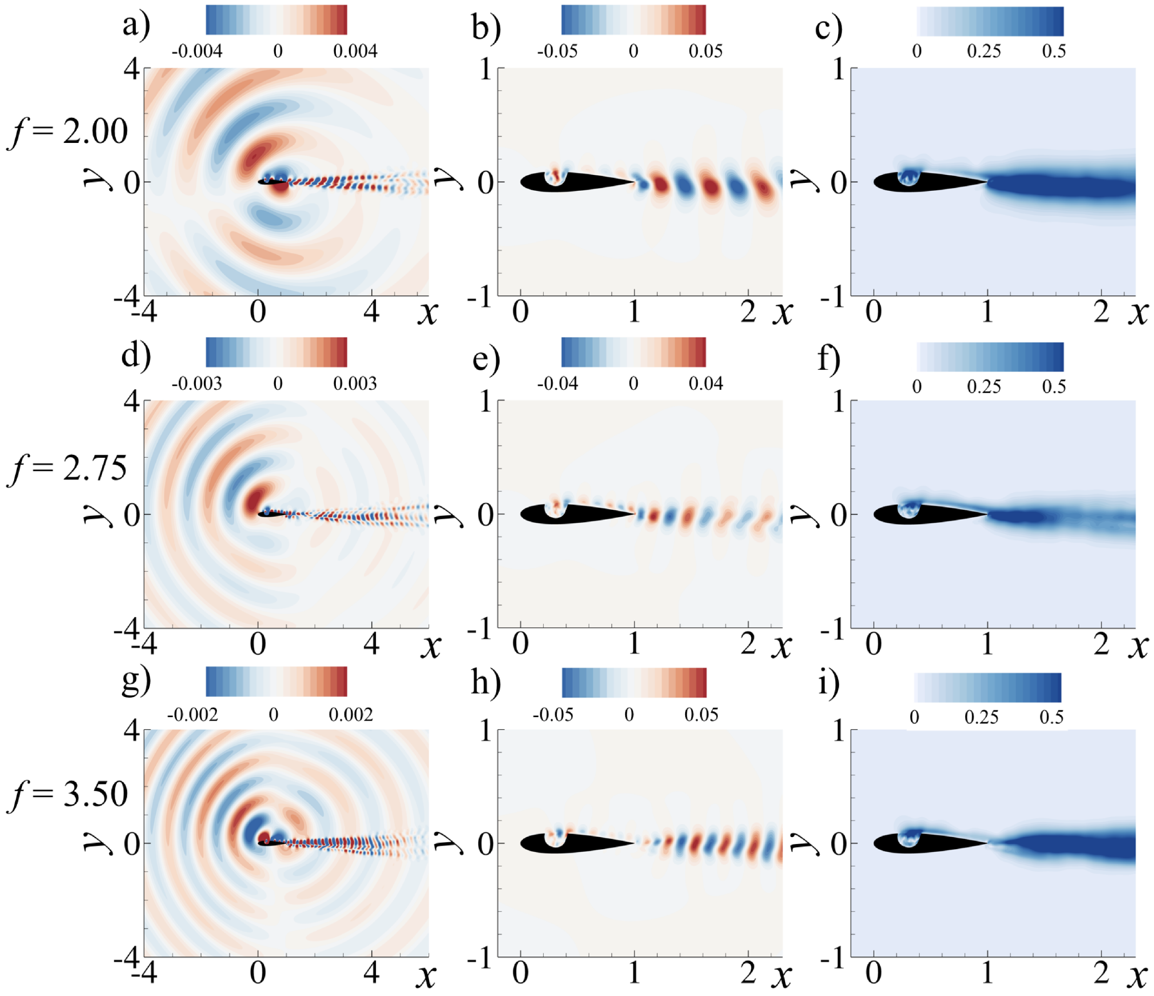

Fig. 20 Type III acoustic generation in CAV. a) - c) Instantaneous p', instantaneous v' and $|v'|/|v'|_{max}$ at $f = 2.00$; d) - f) instantaneous p', instantaneous v' and $|v'|/|v'|_{max}$ at $f = 2.75$; g) - i) instantaneous p', instantaneous v' and $|v'|/|v'|_{max}$ at $f = 3.50$.

airfoil. The modifications greatly enhance the lift coefficient as a result of substantial reduction in the average pressure on the upper airfoil surface. Secondly, the drag coefficient shows a slight reduction, but its fluctuation grows stronger. All these changes lead to a significant increase in the mean lift-to-drag ratio from almost zero to 5.3.

Vortex shedding from the airfoil trailing edge is an important source of flow unsteadiness in both cases. In the absence of a cavity, a low frequency wake flapping prevails. Wavelet analysis near the airfoil trailing edge confirms the switching between the fundamental vortex shedding frequency and its first harmonic. The frequency of the vortex shedding decreases slightly in the presence of the cavity. One also observes a jittering of the flow under the influence of flow disturbances convected from the cavity. Besides, the cavity induces various oscillations within the shear layer covering the cavity, but those oscillations bear only a weak resemblance to the Rossiter modes of the cavity flow. Switching between the first and second shear layer modes in the cavity is also observed and is consistent with the literature. One should note that the first shear layer mode in the cavity appears to be less vigorous than that observed in the experiment, implying a milder interaction between the cavity shear layer and the cavity. As suggested in the literature, such difference may be attributed to the modulation of the flow by three-dimensional instability of the recirculating flow in the cavity and by the boundary layers at the spanwise end of the cavity. Wavelet analysis shows that the mode switching is not limited to those two shear layer modes, but also extends to other frequencies such as the frequency of the airfoil vortex shedding and other frequencies involving aeroacoustic feedback mechanisms and the airfoil boundary layer.

In regard to sound generation, the ordinary NACA 0018 airfoil without any cavity shows a symmetric directivity pattern about the airfoil chord with a preferential radiation toward the upstream direction. A silent zone exists ahead of the airfoil. The introduction of cavity reduces the sound generation from the lower airfoil surface. Scattering at the airfoil leading edge and trailing edge is also observed. One of the most interesting observations is that the introduction of the cavity effectively reduces the production of acoustic power by 1.2 dB and 2.6 dB respectively from the airfoil upper and lower surfaces even if the contribution of low-frequency wake flapping of ordinary airfoil is not counted. This comparison presents a conservative scenario which evidently highlights the noise benefit gained from installing a cavity in the airfoil. To further explore the reasons behind the acoustic power reduction, the whole field FFT filtering and coherence analysis between the far field acoustics and near field velocity fluctuation along the boundary layer of the airfoil are performed. Three major acoustic generation mechanisms are identified from the results. They are (I) the vortex shedding from the airfoil trailing edge, (II) the shear layer oscillation of the cavity, and (III) the aeroacoustic feedback loop involving the boundary layer spanning from the cavity trailing edge and the airfoil trailing edge. All the outcomes of the present study clearly show that an airfoil with a cavity is a feasible configuration that gives high lift-to-drag ratio yet low noise generation, making it a promising quiet airfoil design at low Reynolds number.

Acknowledgment

The authors gratefully acknowledge the support given by the Central Research Grant of The Hong Kong Polytechnic University under grant nos. G-YL56 and G-YBGF. The second author acknowledges the support with a research donation from Philip K. H. Wong Foundation under grant no. 5-ZH1X, and a research project given by the State Key Laboratory of Mechanical System and Vibration of Shanghai Jiao Tong University under grant no. MSV201404.

References

[1] Mueller, T. J. and DeLaurier, J. D., “Aerodynamics of small vehicles,” *Annual Review of Fluid Mechanics*, Vol. 35, No. 1, 2003, pp. 89–111.

[2] Boutilier, M. S. and Yarusevych, S., “Parametric study of separation and transition characteristics over an airfoil at low Reynolds numbers,” *Experiments in Fluids*, Vol. 52, No. 6, 2012, pp. 1491–1506.

[3] Nakano, T., Fujisawa, N., and Lee, S.,“Measurement of tonal-noise characteristics and periodic flow structure around NACA0018 airfoil,” *Experiments in Fluids*, Vol. 40, No. 3, dec 2005, pp. 482–490.

[4] Kasper, W., U. S. Patent Application for “Aircraft wing with vortex generation,” Patent No. US3831885, filed 11 Jul. 1972.

[5] Chernyshenko, S. I., Galletti, B., Iollo, A., and Zannetti, L., “Trapped vortices and a favourable pressure gradient,” *Journal of Fluid Mechanics*, Vol. 482, 2003, pp. 235–255.

[6] Savitsky, A. I., Schukin, L. N., Karelin, V. G., Mass, A. M., Pushkin, R. M., Shibanov, A. P., Schukin, I. L., and Fischenko, S. V., U. S. Patent Application for “Method for control of the boundary layer on the aerodynamic surface of an aircraft, and the aircraft provided with the boundary layer control system,” Patent No. US5417391, filed 3 Jun. 1993.

[7] Bunyakin, A. V., Chernyshenko, S. I., and Stepanov, G. Y., “Inviscid Batchelor-model flow past an airfoil with a vortex trapped in a cavity,” *Journal of Fluid Mechanics*, Vol. 323, 1996, pp. 367–376.

[8] Bunyakin, A. V., Chernyshenko, S. I., and Stepanov, G. Y., “High-Reynolds-number Batchelor-model asymptotics of a flow past an aerofoil with a vortex trapped in a cavity,” *Journal of Fluid Mechanics*, Vol. 358, 1998, pp. 283–297.

[9] Iollo, A. and Zannetti, L., “Trapped vortex optimal control by suction and blowing at the wall,” *European Journal of Mechanics, B/Fluids*, Vol. 20, No. 1, 2001, pp. 7–24.

[10] Lasagna, D., Donelli, R., De Gregorio, F., and Iuso, G., “Effects of a trapped vortex cell on a thick wing airfoil,” *Experiments in Fluids*, Vol. 51, No. 5, 2011, pp. 1369–1384.

[11] Tutty, O., Buffoni, M., Kerminbekov, R., Donelli, R., De Gregorio, F., and Rogers, E., "Control of Flow with Trapped Vortices: Theory and Experiments," *International Journal of Flow Control*, Vol. 5, No. 2, 2013, pp. 89–110.

[12] Olsman, W. F. J., Willems, J. F. H., Hirschberg, A., Colonius, T., and Trieling, R. R., "Flow around a NACA0018 airfoil with a cavity and its dynamical response to acoustic forcing," *Experiments in Fluids*, Vol. 51, No. 2, 2011, pp. 493–509.

[13] Olsman, J. W. F. and Colonius, T., "Numerical Simulation of Flow over an Airfoil with a Cavity," *AIAA Journal*, Vol. 49, No. 1, 2011, pp. 143–149.

[14] Schumacher, K. L., Doolan, C. J., and Kelso, R. M., "The effect of a cavity on airfoil tones," *Journal of Sound and Vibration*, Vol. 333, No. 7, 2014, pp. 1913–1931.

[15] Lam, G. C. Y., Leung, R. C. K., Seid, K. H., and Tang, S. K., "Validation of CE/SE Scheme in low Mach number direct aeroacoustic simulation," *International Journal of Nonlinear Sciences and Numerical Simulation*, Vol. 15, No. 2, 2014, pp. 157–169.

[16] Lam, G. C. Y., Leung, R. C. K., and Tang, S. K., "Aeroacoustics of duct junction flows merging at different angles," *Journal of Sound and Vibration*, Vol. 333, No. 18, 2014, pp. 4187–4202.

[17] Arcondoulis, E. J. G., Doolan, C. J., Zander, A. C., and Brooks, L. A., "A review of trailing edge noise generated by airfoils at low to moderate Reynolds number," *Acoustics Australia*, Vol. 38, No. 3, 2010, pp. 129 – 133.

[18] Ikeda, T., Atobe, T., and Takagi, S., "Direct simulations of trailing-edge noise generation from two-dimensional airfoils at low Reynolds numbers," *Journal of Sound and Vibration*, Vol. 331, No. 3, 2012, pp. 556–574.

[19] Loh, C. Y., and Zaman, K. B. M. Q. , "Numerical investigation of transonic resonance with a convergent-divergent nozzle," *AIAA Journal*, Vol. 40, No. 12, 2002, pp. 2393–2401.

[20] Loh, C. Y., and Hultgren, L. S. , 'Jet Screech Noise Computation," *AIAA Journal*, Vol. 44, No. 5, 2006, pp. 992–998.

[21] Olsman, J. W. F. and Colonius, T., "Influence of a cavity on the dynamical behaviour of an airfoil," *PhD. thesis*, Universiteitsdrukkerij TU Eindhoven, 2010, pp. 131–133.

[22] Drela, M., "XFOIL: An Analysis and Design System for Low Reynolds Number Airfoils," *Low Reynolds Number Aerodynamics*, edited by T. Mueller, Lecture Notes in Engineering, Vol. 54, Springer, Berlin, Heidelberg, 1989, pp. 1–12.

[23] Michalke, A., "On spatially growing disturbances in an inviscid shear layer," *Journal of Fluid Mechanics*, Vol. 23, No. 03, 1965, pp. 521.

[24] Rossiter, J. E., “Wind tunnel experiments on the flow over rectangular cavities at subsonic and transonic speeds,” Royal Aircraft Establishment Technical Report, , No. 64037, 1964.

[25] Heller, H., Holmes, D., and Covert, E., “Flow-induced pressure oscillations in shallow cavities,” *Journal of Sound and Vibration*, Vol. 18, No. 4, 1971, pp. 545–553.

[26] Terracol, M., and Manoha, E., and Lemoine, B., “Investigation of the unsteady flow and noise generation in a slat cove,” *AIAA Journal*, Vol. 54, No. 2, 2016, pp. 469–489.

[27] Bauer, R. C. and Dix, R. E., “Engineering model of unsteady flow in a cavity,” AEDC-TR-91-17, 1991.

[28] Torrence, C. and Compo, G. P., “A Practical Guide to Wavelet Analysis,” *Bulletin of the American Meteorological Society*, Vol. 79, No. 1, 1998, pp. 61–78.

[29] Farge, M., “Wavelet Transforms and their Applications to Turbulence,” *Annual Review of Fluid Mechanics*, Vol. 24, No. 1, 1992, pp. 395–458.

[30] Larchevêque, L., Sagaut, P., Mary, I., Labbé, O., and Comte, P., “Large-eddy simulation of a compressible flow past a deep cavity,” *Physics of Fluids*, Vol. 15, No. 1, 2003, pp. 193–210.

[31] Larchevêque, L., Sagaut, P., Lê, T.-H., and Comte, P., “Large-eddy simulation of a compressible flow in a three-dimensional open cavity at high Reynolds number,” *Journal of Fluid Mechanics*, Vol. 516, 2004, pp. 265–301.

[32] Arbey, H. and Bataille, J., “Noise generated by airfoil profiles placed in a uniform laminar flow,” *Journal of Fluid Mechanics*, Vol. 134, 1983, pp. 33.